March 2021 volume 3 no. 3
www.nature.com/natrevphys

# nature reviews physics

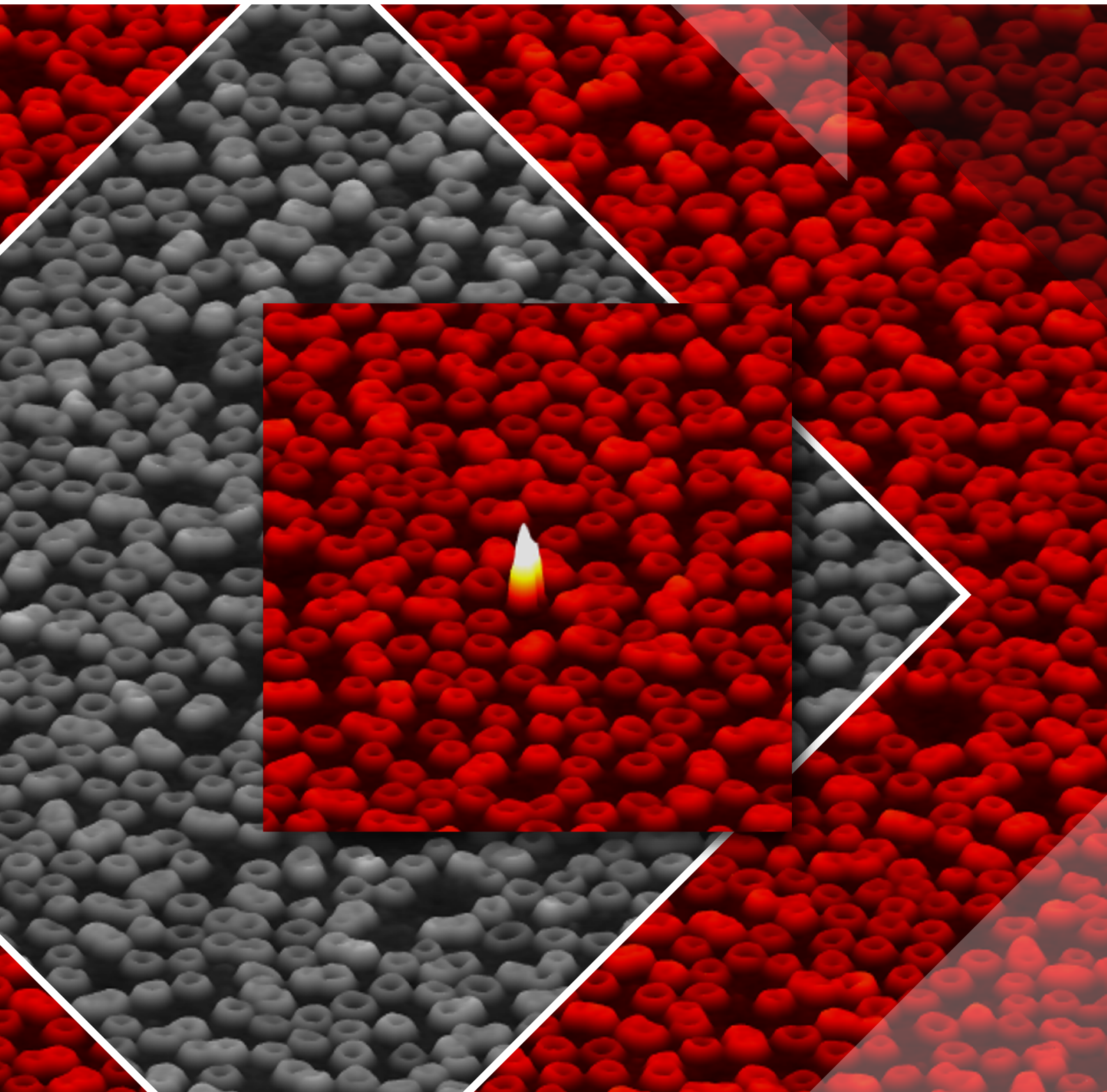

TECHNICAL REVIEWS



# Concept, implementations and applications of Fourier ptychography

*Guoan Zheng*[1]✉, *Cheng Shen*[2], *Shaowei Jiang*[1], *Pengming Song*[1] and *Changhuei Yang*[2]✉

Abstract | The competition between resolution and the imaging field of view is a long-standing problem in traditional imaging systems — they can produce either an image of a small area with fine details or an image of a large area with coarse details. Fourier ptychography (FP) is an approach for tackling this intrinsic trade-off in imaging systems. It takes the challenge of high-throughput and high-resolution imaging from the domain of improving the physical limitations of optics to the domain of computation. It also enables post-measurement computational correction of optical aberrations. We present the basic concept of FP, compare it to related imaging modalities and then discuss experimental implementations, such as aperture-scanning FP, macroscopic camera-scanning FP, reflection mode, single-shot set-up, X-ray FP, speckle-scanning scheme and deep-learning-related implementations. Various applications of FP are discussed, including quantitative phase imaging in 2D and 3D, digital pathology, high-throughput cytometry, aberration metrology, long-range imaging and coherent X-ray nanoscopy. A collection of datasets and reconstruction codes is provided for readers interested in implementing FP themselves.

How much information does a microscope transmit? This question can be quantitatively answered through the use of a concept known as the space–bandwidth product (SBP)[1]. The SBP characterizes the total number of effective independent pixels over a system's field of view (FOV). It can be interpreted as the effective information channel bandwidth for image data collection through a physical system. Most off-the-shelf objective lenses have SBPs of ~10 megapixels, regardless of their magnification factors or numerical apertures (NAs). For example, a standard 20×, 0.4 NA microscope objective lens has a resolution of ~0.8 µm and a FOV of ~1.1 mm in diameter, corresponding to an SBP of ~6 megapixels. A high SBP is very much desired in microscopy.

One strategy for increasing the SBP of a microscope system is to make the lens larger. Unfortunately, doing so also increases the associated aberrations. In imaging systems, this issue is partially addressed by increasing the number of optical surfaces in order to correct the increased aberrations. As a point of reference, extreme ultraviolet (EUV) lithography platforms are designed based on this engineering principle and they can have an NA of 0.33 and a FOV of 26 mm by 33 mm. This corresponds to an SBP of thousands of gigapixels in the EUV regime. Similarly, giant objective lenses have been designed for the visible wavelengths[2,3], and they have shown great promises on high-throughput, large-scale microscopy applications. However, the required number of optical surfaces leads to an expensive, bulky and highly specialized design. These lenses and the related set-ups are not readily available to the average researcher for cost reasons and because they are highly specialized and designed to work within a tightly controlled usage tolerance range.

Fourier ptychography (FP) was developed to expand the SBP of a regular microscope platform without major hardware modifications. The original FP set-up[4] was modified from an LED array microscope designed for 3D tomographic imaging[5]. The set-up uses a conventional upright microscope with a 2×, 0.08-NA objective lens. An off-the-shelf LED array beneath the microscope provides illumination of the object from a series of different incident angles. At each angle, the system records a low-resolution intensity image that corresponds to the information from a circular pupil aperture in the Fourier domain (BOX 1). The size of the aperture is determined by the NA of the objective and its offset from the origin is determined by the illumination angle. All captured images are then synthesized in the Fourier domain in an iterative phase retrieval process. The synthesized information in the Fourier domain is used to generate a high-resolution, complex-valued object image that includes both intensity and phase properties. It also retains the original large FOV set by the low-NA objective lens[4,6].

[1]*Department of Biomedical Engineering, University of Connecticut, Storrs, CT, USA.*

[2]*Department of Electrical Engineering, California Institute of Technology, Pasadena, CA, USA.*

✉*e-mail: guoan.zheng@uconn.edu; chyang@caltech.edu*

https://doi.org/10.1038/s42254-021-00280-y

**Key points**

- Fourier ptychography (FP) is a computational method for synthesizing raw data into a high-resolution and wide-field-of-view image through a combination of synthetic aperture and phase retrieval concepts. Unlike conventional techniques, which trade resolution against imaging field of view, FP can achieve both simultaneously.
- FP can computationally render both the intensity and the phase images of the sample from intensity-based measurements.
- FP has the intrinsic ability to computationally correct aberrations. As a result, in FP, the task of aberration correction is not a physical system design problem but, rather, a computational problem that can be resolved post-measurement.
- Defocus is a type of aberration and, thus, FP can computationally refocus images over a much extended range.
- Since the invention of FP, various innovations on the original method have been reported; this Technical Review discusses some of the most impactful ones, such as aperture-scanning and camera-scanning schemes, extensions for handling 3D specimens and X-ray FP, among others.
- A collection of FP datasets and reconstruction codes is provided to interested readers.

Since its demonstration in 2013, FP has evolved from a simple microscope tool to a general technique for different research communities. Some of the FP developments were rather unexpected. These surprising developments include a lens-scanning scheme that deviates from microscopy and enables far-field super-resolution imaging[7,8], an X-ray implementation that demonstrates unexpected dose efficiency[9] and the integration of FP with tomography for high-resolution 3D microscopy[10,11]. In this Technical Review, we first present the basic concept of FP and discuss its connections with the related real-space ptychography approach. We then review different implementation schemes and discuss related applications. Finally, we discuss the existing challenges and future directions for development.

## Fourier ptychography and its related modalities

The FP method integrates two innovations in classical optics: synthetic aperture imaging[12] and phase retrieval[13,14]. Synthetic aperture imaging was first developed at radio wavelengths, with the goal of bypassing the resolution limit of a single radio telescope. The method combines images from several telescopes — a feasible task if both phase and intensity information are known. FP employs the same design strategy: synthesizing the pupil aperture at the Fourier plane to bypass the resolution set by the objective lens. However, with FP, no phase is directly measured during the acquisition process, thereby eliminating the challenges of direct phase measurements, as exist in holography. Instead, FP recovers the missing phase from intensity measurements using an iterative phase retrieval process (BOX 1). This process uses many low-resolution intensity measurements as constraints on a high-resolution, complex-valued object solution. In the original FP implementation[4], this solution was recovered using the alternating projection algorithm. In brief, the estimated solution is alternatively projected to two constraint sets in the recovery process. In the spatial domain, the captured images are used to constrain the modulus. In the Fourier domain, the confined pupil apertures are used as the support constraints. BOX 1 gives a brief introduction to the alternating projection process with one incident angle, as well as an intuitive explanation about the constraints. For FP, this process is repeated for multiple images captured under different incident angles. Varying the incident angle effectively pans the confined pupil aperture across the Fourier space, in effect synthesizing a large passband for the complex object (FIG. 1). BOX 2 and the Supplementary Note provide a simple protocol for setting up an FP experiment using off-the-shelf components.

As suggested by its name, FP is closely related to an imaging modality termed ptychography (the 'p' is silent; here, we refer to it as real-space ptychography for distinction[15]). The name ptychography derives from the Greek 'ptycho', meaning 'to fold'. Real-space ptychography originates from electron microscopy and is a lensless imaging technique that was introduced to solve the phase problem[16]. It does so by using the convolution theorem to recover phase information from diffraction measurements. Present-day implementations of this technique were brought to fruition with the help of iterative phase retrieval algorithms[17–24]. For a detailed discussion of the history and different implementations of ptychography, we direct interested readers to REF.[25].

Real-space ptychography typically illuminates the object with a spatially confined beam, and the object is mechanically translated. The captured Fourier diffraction patterns are recorded in the far field, and, from them, the complex object image in real space is recovered. FP and real-space ptychography share the same forward imaging model (FIG. 1). In real-space ptychography, the finite support constraint is imposed by the confined probe beam in the spatial domain, whereas the modulus constraint is imposed by the diffraction measurement in the Fourier domain. By contrast, FP uses a lens and, thereby, swaps the spatial and Fourier domains[4,26]. In FP, the finite support constraint is imposed by the pupil aperture in the Fourier domain, whereas the modulus constraint is imposed by the image measurement in the spatial domain. For both techniques, data redundancy via aperture overlap between adjacent acquisitions is critical for a successful reconstruction. If no overlap is imposed, the recovery process is carried out independently for each acquisition, leading to the usual ambiguities inherent to the phase problem. The imaging model in FIG. 1 also suggests the use of spatially coherent light sources for both techniques. In practice, a light source incoherently emits photons across a finite region. According to the van Cittert–Zernike theorem, one way to improve spatial coherence is to place the source far away from the sample, in effect reducing the optical flux reaching the sample. Alternatively, the finite extent of the light source can be divided into multiple coherent point sources. The resulting intensity pattern can, therefore, be treated as an incoherent summation of multiple diffraction patterns from these point sources, that is, an incoherent mixture of coherent states. One can then model this mixture as multiple incoherent modes of pupil($k_x$, $k_y$) in FP (where $k_x$ and $k_y$ are wavenumbers in the $x$ and $y$ directions, respectively); the real-space ptychography analogue is probe($x$, $y$)[23]. In general, the partial spatial coherence of LED light sources can be well addressed in both FP and real-space ptychography[27].

Box 1 | **Phase retrieval and alternating projection**

Phase information characterizes the optical delay accrued during propagation. This information is typically lost in the detection process, because light detectors measure intensity-only variations. The phase information can be regained at the cost of greater experimental complexity, typically by requiring light interference with a known field, in the process of holography. An alternative means of measuring phase — without requiring interferometric set-ups — is phase retrieval.

We consider an optical microscope set-up (see the figure, panel **a**). In this set-up, the operations of the objective and the tube lens are to sequentially perform two Fourier transforms, denoted as FT, of the object's light waves. Panel **b** of the figure shows the acquisition process. First, the complex-valued object $O(x, y)$ interacts with the tilted plane wave $e^{ik_{xi}x}e^{ik_{yi}y}$, generating an exit field $O(x, y) \cdot e^{ik_{xi}x}e^{ik_{yi}y}$, where $k_{xi}$ and $k_{yi}$ are wavenumbers in the $x$ and $y$ directions, respectively. Second, the objective performs a Fourier transform of this field: $\mathrm{FT}\{O(x, y) \cdot e^{ik_{xi}x}e^{ik_{yi}y}\} = \hat{O}(k_x - k_{xi}, k_y - k_{yi})$. Third, the resulting spectrum is low-pass filtered by the pupil aperture with a cut-off frequency of $\mathrm{NA} \cdot 2\pi/\lambda$, where NA is the numerical aperture and $\lambda$ is the light wavelength. Finally, the tube lens performs a second Fourier transform of the filtered spectrum $\hat{O}_{\mathrm{fil}}$ and the resulting intensity image $I(x, y)$ is captured by the detector.

The phase retrieval process in this example is to recover the complex object $O(x, y)$ from the intensity measurement $I(x, y)$. One effective algorithm for this problem is alternating projection[13], which finds the intersection between two sets of solutions (see the figure, panel **c**). The first set is all possible object solutions that are constrained within a given support area, termed the constraint set. In this example, the support area is the pupil aperture in the Fourier domain. Signals outside this area are blocked off by the aperture. To impose this support constraint, one can set the signals outside the support area to 0 s, while keeping the signals inside the area unchanged. The second set is all possible object solutions that are consistent with the given intensity measurement, termed the modulus set. The search for the intersection is performed by projecting the current estimate onto these two sets (see the figure, panel **c**). In our example, projecting to the constraint set is performed in the Fourier domain by setting the spectrum values outside the shifted pupil aperture to 0s. The shifted offset $(-k_{xi}, -k_{yi})$ is determined by the illumination wavevector. By contrast, projecting to the modulus set is performed in the spatial domain by replacing the modulus of the estimated object $O'(x, y)$ with $\sqrt{I(x, y)}$, while keeping the phase unchanged. Panel **d** of the figure shows the alternating projection process. First, the initial guess of the complex object $O'(x, y) = \sqrt{I(x, y)}$ is projected to the constraint set in the Fourier domain by setting the spectrum values outside the shifted pupil aperture to 0 s. Second, the updated spectrum is transformed back to the spatial domain and the object amplitude is replaced by the measurement, while the phase is kept unchanged. The above two projections are repeated until the solution converges.

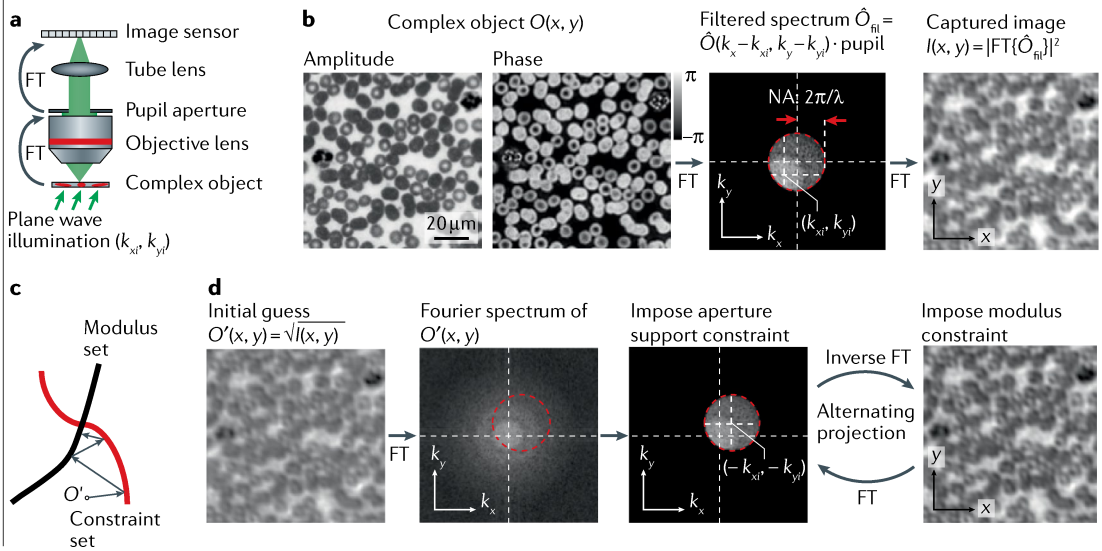


Because real-space ptychography and FP are closely related, conceptual innovations developed for real-space ptychography can be adopted for FP. For example, the coherent-state multiplexing scheme[23,24], multi-slice modelling[28], the positional correction scheme[29] and the object-probe recovery scheme[19,20] can be directly implemented in FP experiments. Despite the close relationship between the two techniques, they have different strengths and weaknesses. As summarized in FIG. 1, a key difference is that FP provides a straightforward means for resolution improvement. To date, the best reported NA is ~1.6 for FP[30] and ~0.4 for lensless real-space ptychography[27,31]. Other differences include the impact of the dynamic range of the detector on the final image quality, differing temporal coherence requirements, sampling strategies and initialization strategies. We also note that there is a related implementation of angle-varied illumination for resolution improvement in electron microscopy, known as tilted series reconstruction[32,33]. To the best of our knowledge, Fourier aperture synthesizing via iterative phase retrieval had not been demonstrated until FP was developed.

## Implementations of Fourier ptychography

***Strategies for improving performance.*** TABLE 1 categorizes different FP implementations into four groups. FIGURE 2 shows some of the representative schematics of these implementations. The first group of implementations

is related to performance improvement of the original LED array microscope set-up. Here, we discuss strategies for improving the resolution, acquisition speed, device portability and phase imaging capability.

The resolution $d$ of the complex amplitude in an FP system is determined by both the NA of the objective lens ($NA_{obj}$) and the maximum illumination NA of the LED array ($NA_{illumination}$): $d = \lambda/(NA_{obj} + NA_{illumination})$, where $\lambda$ is the wavelength of the illumination. The reported resolution of complex amplitude for coherent imaging methods, which include FP, is much confused by the existence of varying definitions, leading to over- and under-reporting of resolution. Interested readers can refer to a standardized method for reporting and comparing resolution[34].

From the equation, it is clear that higher FP resolution can be achieved by either increasing the objective NA or using an LED array with larger incident angles[30,35–38]. The first high-NA FP system was demonstrated using a 40×, 0.75-NA objective and a maximum illumination NA of 0.7 to synthesize a system NA of 1.45 (REF.[35]). Similarly, a 1.6-NA FP system was demonstrated using a 10×, 0.4-NA objective and a 1.2-NA oil-immersion condenser lens[30].

The original FP set-up has an acquisition speed that is limited by a large number of image acquisitions and the relatively long exposure time for acquiring the darkfield images. To reduce the number of acquisitions, better sampling strategies can be employed by selecting or arranging the LED illumination wavevectors ($k_{xi}$, $k_{yi}$) in the Fourier space (index $i$ refers to the $i$th LED element; $i = 1, 2, \ldots$). One example is content-adaptive illumination[39–41], in which a subset of illumination angles is selected based on the spectral energy distribution in the Fourier space. This strategy is most effective for specimens that have a highly structured Fourier spectrum, such as the

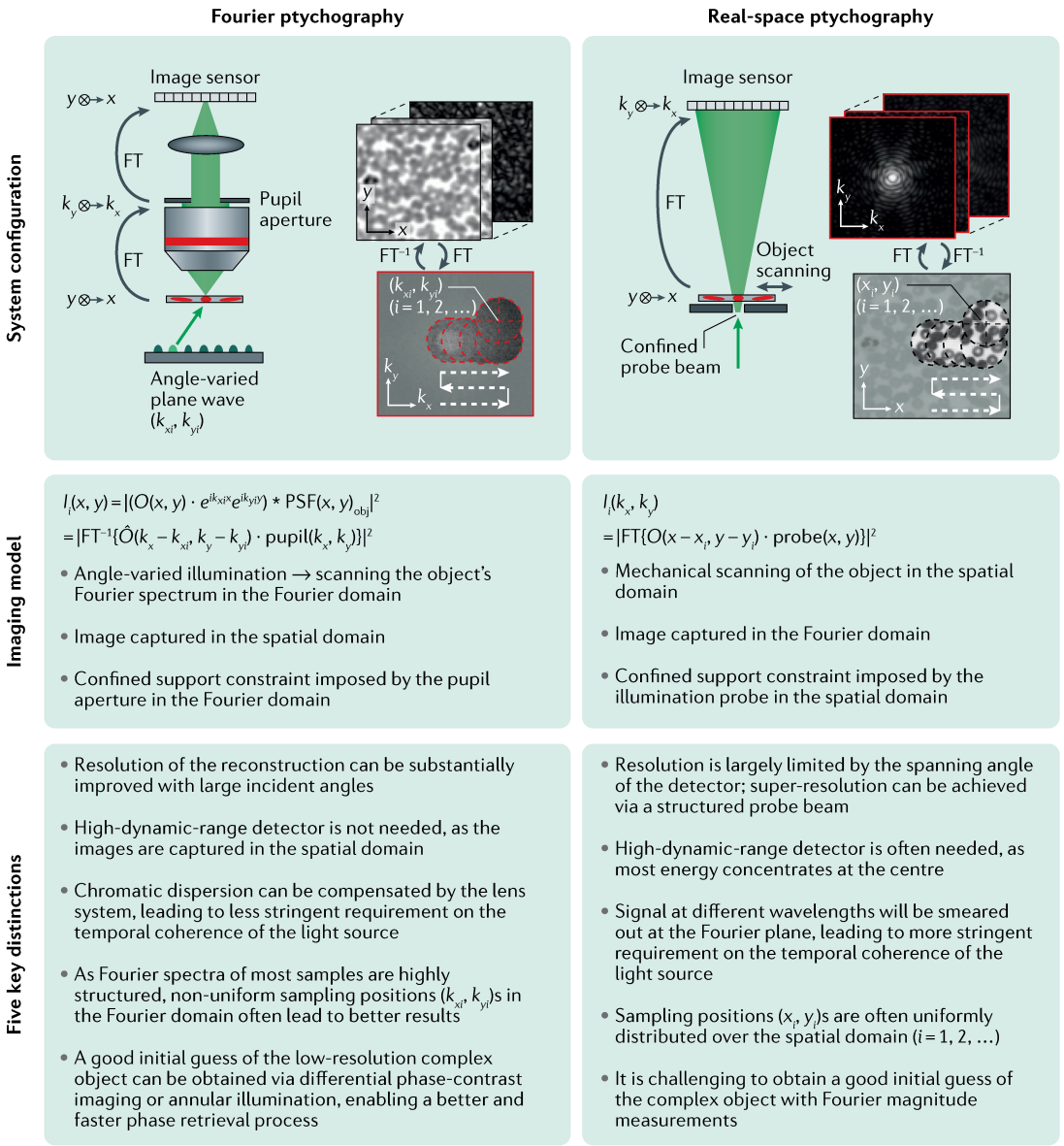


Fig. 1 | **Comparison between Fourier ptychography and real-space ptychography.** FT, Fourier transform; $k$, wavevector; $I_i(x, y)$, the $i$th captured image in the spatial domain; $I_i(k_x, k_y)$, the $i$th captured image in the Fourier domain; $O(x, y)$, the complex object profile; $PSF(x, y)$, the point spread function of the imaging system.

Box 2 | **Setting up a Fourier ptychography experiment and a collection of Fourier ptychography datasets**

To set up a simple Fourier ptychography (FP) experiment, one can place an LED array under the specimen in a microscope platform (see the figure, panel **a**; also refer to the Supplementary Note). In the image acquisition process, an empty slide can be used to collect the reference darkfield images for background correction (darkfield refers to the scenario in which the LED illumination angle exceeds the maximum acceptance angle of the objective). The subtraction of these reference darkfield images from measurements can reduce the impacts of ambient and stray light.

To infer the position of the LED array with respect to the specimen, we can select an LED element as the central reference point. Four adjacent centrosymmetrical LEDs are then chosen such that their incident angles are close to the maximum acceptance angle of the objective. Thus, the captured image corresponding to these four LEDs exhibits brightfield-to-darkfield transition features (see the figure, panel **b**). The location and the orientation of the LED array can be estimated from these features.

In the iterative phase retrieval process, the captured images are often segmented into small tiles (such as 256 × 256 pixels) for reconstruction. In this way, the pupil aberration can be treated as spatially invariant across the area of each tile, and the LED illumination can be assumed to be planar. Some regions of the captured images are better to be excluded from updating the object solution. Panels **c** and **d** of the figure demonstrate two representative cases: the brightfield-to-darkfield transition region and the bright spot caused by stray light. As shown in the insets of panels **c** and **d**, binary masks can be generated to locate these regions. When the corresponding images are used as modulus constraints in the updating process, the pixels in the masked white regions are not used to update the estimated object solution[131]. A collection of 11 FP datasets and reconstruction codes is provided for interested readers (see the figure, panel **e**; also refer to the 'Code availability' statement).

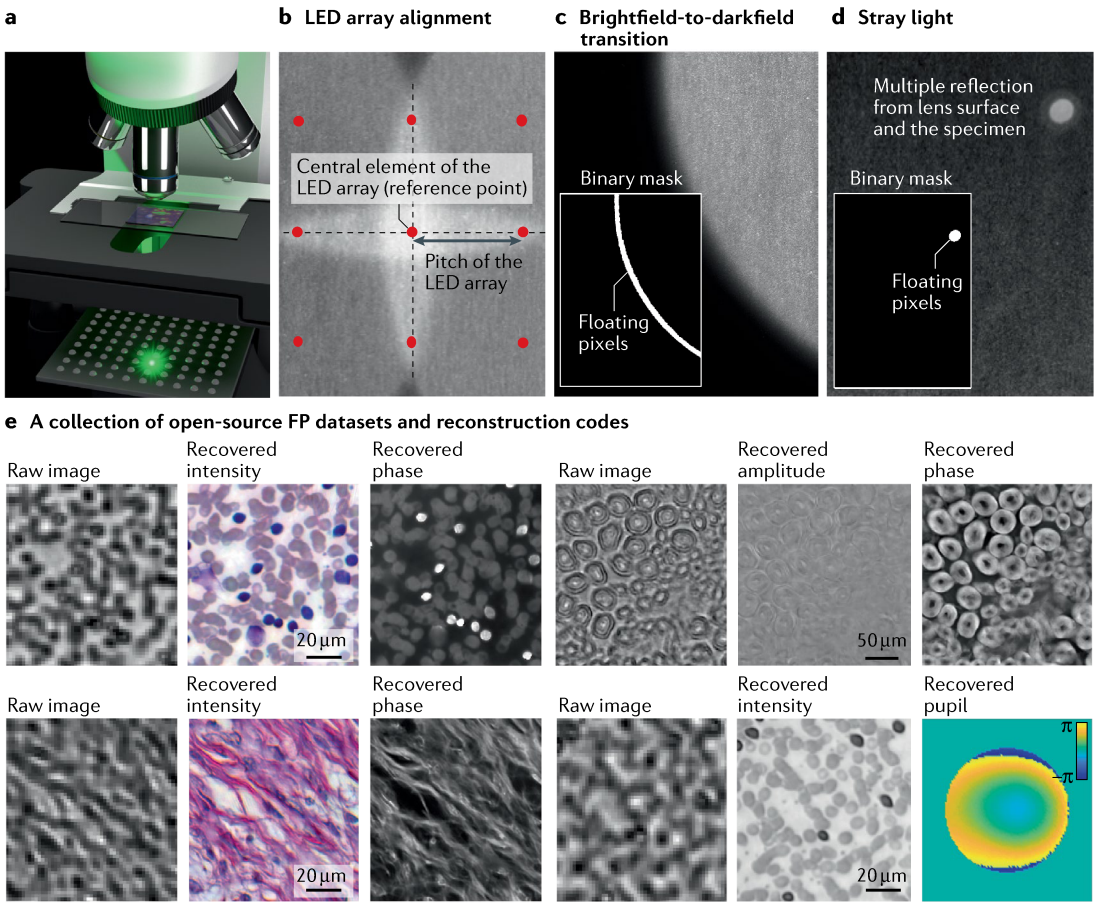


United States Air Force (USAF) resolution target. It may be ineffective for biological samples, the frequency contents of which are often uniformly expanded in the Fourier space. Another strategy for reducing the number of acquisitions is to sample the Fourier domain in a non-uniform manner[42] (left panel of FIG. 2a). As most signal energy concentrates at the central region of the Fourier spectrum, a higher density of sampling points ($k_{xi}$, $k_{yi}$) can be employed for the central region. For darkfield images with large incident angles, the aperture overlap between adjacent acquisitions can be reduced to 20% or less. With the same Fourier bandwidth coverage, this strategy can substantially reduce the number of acquisitions from 137 in the original FP set-up to 68 (REF.[42]). We also note that the sampling points ($k_{xi}$, $k_{yi}$) in the original FP set-up form a quasi-periodic grid in the Fourier domain. Such a periodic scan pattern is susceptible to image artefacts known as the raster scan pathology[19]. A non-uniform sampling strategy can address this issue by breaking the translational symmetry of the sampling points in the Fourier domain. The third method for reducing the number of acquisitions is to perform

Table 1 | **Summary of different Fourier ptychography implementations**

| Class of methods | Examples |
|---|---|
| ***Improving the performance of the original FP implementation*** | |
| Resolution improvements | Larger incident angles[35–38], oil-immersion condenser lens[30] |
| Acquisition speed improvements | Content-adaptive illumination[39–41], non-uniform sampling strategy in the Fourier plane[42], spectral and angular multiplexing[43–46], multiplexed source coding[47], symmetrical illumination[129], rapid laser beam scanning[49–51] |
| System portability improvements | Beam steering via a low-cost liquid crystal display[130], a cellphone lens system[53], a mouldless lens system[120], a Raspberry Pi system[54], a low-cost whole-slide scanner with LED array illumination[55] |
| Phase imaging capability improvements | Better initial guess of phase via differential-phase-contrast imaging[47], annular illumination[43,56] |
| ***Reconstruction approaches and algorithms*** | |
| System corrections | LED intensity correction[57,58], LED alignment calibration and incident angle correction[58–63], correcting underexposed and overexposed pixels[131], joint sample-pupil recovery[65,66,94,121], sample motion correction[132], stray light detection[133], vignetting effect[134] |
| Phase retrieval algorithms | Stochastic gradient descent[65], Gauss–Newton method with amplitude-based cost function[62], adaptive step size for gradient descent[135], Wirtinger gradient[136–140], convex relaxation[124], regularization via sparsity[141,142], noise modelling and denoising[137,138,143,144], stochastic proximal gradient descent[145], low-rank recovery[146] |
| Neural network and related approaches | High-resolution image recovery from low-resolution FP measurements via deep neural networks[68–73], incorporating physical model for designing the coded illumination pattern[74–78], neural network model for the optimization process (also known as automatic differentiation)[79–82], virtual brightfield/fluorescence staining and other unsupervised image style transfer of the FP reconstructions[84] |
| ***New hardware implementations*** | |
| Aperture-scanning FP | Mechanical scanning of a confined aperture[7,87,94] and a diffuser[86], digital scanning via a spatial light modulator[85,121,128], dual-wavelength implementation for phase unwrapping[87], single-shot implementation[88] |
| Long-range super-resolution imaging | Camera-scanning FP[7,8,89] |
| Reflective implementations | Angle-varied illumination[90–93,95], aperture scanning[87,94] |
| Multiple cameras | Six cameras[119] and 96 cameras[96] for parallel acquisition, Scheimpflug arrangement[97] |
| Single-shot implementations | Diffraction grating[88,99], lens array[98], colour multiplexing[43] |
| Translated speckle illumination | Fluorescence[101,102,104], coherent imaging[103,104], far-field speckle scanning for long-range super-resolution imaging[103,105] |
| X-ray imaging | Pinhole scanning[9], lens and detector translation[9,106,107], Bragg configuration[108] |
| ***Addressing model limitations: 2D wave-object multiplication*** | |
| Better forward imaging model | Multi-slice modelling[15,111,112], diffraction tomography[10,11,147–150] |
| Modulating the exit wave at the detection path | Aperture-scanning FP[7,85–87,94], diffuser modulation for coherent super-resolution microscopy[113,114] |

FP, Fourier ptychography.

multiplexed sampling in the Fourier domain. In this case, multiple LEDs with different incident angles[43,44] or different colours[43,45,46] can be turned on at the same time for sample illumination (FIG. 2b). A high-speed FP implementation[47] using this strategy has been demonstrated for in vitro applications (right panel of FIG. 2b). In this implementation, an initial guess of the complex object was generated via differential-phase-contrast imaging[48], which was performed by turning on half of the LED array for image acquisitions. With a good initial guess, it is possible to recover the high-resolution complex object with multiplexed darkfield measurements.

The use of the LED array in the original FP set-up leads to a relatively long exposure time for acquiring the darkfield images. To improve the light delivery efficiency, the LED elements can also be angled towards the sample or arranged on a hemispherical dome[36–38] (FIG. 2a, right panel). Another strategy to shorten the exposure time is to replace the LED array with a steerable laser beam for sample illumination[49–51]. The use of laser allows the intensity to be substantially increased beyond the limitation of LEDs. To this end, the use of a guided laser beam for angle-varied illumination has been demonstrated for shortening the acquisition time[50]. In this scheme, a mirror array and a 2D galvo scanner are used to provide plane wave illuminations with centimetre beam size at diverse incidence angles (FIG. 2c, left panel). Similarly, a digital mirror device can be coded to generate angle-varied illumination in high speed[49,51] (FIG. 2c, right panel). In this case, the beam

size and the FOV is limited by the projection lens. For low-light applications, single-photon detection can also be employed in FP to reduce the exposure time and improve the signal-to-noise ratio[52].

The FP approach can be implemented in portable and turnkey systems. For example, low-cost lenses can be used to develop high-resolution imaging systems. Examples include a 3D-printed, field-portable FP microscope using a cellphone lens[53] and an FP microscope with sub-micrometre resolution using a Raspberry Pi and its low-cost camera module[54]. The FOV of most FP implementations discussed so far is limited by the size of the image sensor. The FOV of an FP system can be expanded by integrating a robotic scanning system, as has been demonstrated in a low-cost whole slide scanner using an LED array for sample illumination[55]. It can be used for both regular incoherent microscopy and coherent FP imaging.

The phase retrieval process generally requires a good initial guess. In FP, this initial guess can be created using the captured low-resolution images with the phase set to a constant[4]. In recent years, there have been innovations improving the initial guess. Using differential-phase-contrast imaging[48] to generate the initial phase leads to an improved initialization[47]. Another strategy uses annular illumination[43,56]. In this approach, the illumination angle is close to the maximum acceptance angle of the objective, that is, images are captured near the brightfield-to-darkfield transition region. The phase information of the specimen, especially for the low-frequency phase components, can be effectively converted into intensity variations for detection[56].

***Reconstruction approaches and algorithms.*** A successful FP reconstruction relies on an accurate imaging model of the optical system. Three common system imperfections of an FP set-up can be corrected in the iterative reconstruction process: LED intensity variations, incident angles of the LED elements and pupil aberrations.

LED intensity variations can be corrected using an image-quality metric to update the LED intensity during the iterative reconstruction process[57]. The same metric can also be used to recover the Zernike modes of the pupil aberration. For correcting incident angles from different LED elements, simple alignment of the LED array can be performed following the procedure discussed in BOX 2. This alignment procedure is often sufficient for LED arrays that have a well-defined pitch. For other illuminators without a well-defined pitch, further refinement of the illumination wavevector is needed in the iterative recovery process[58–63]. This wavevector refinement process is similar to the positional correction process in real-space ptychography[29]. For pupil aberration correction, one can directly measure the spatially varying aberrations using a calibration target[64]. Another solution is to jointly recover both the object and the pupil in the iterative process[65]. The field-dependent nature of the optical pupil can also be leveraged for a more robust full-field aberration recovery[66].

Different phase retrieval algorithms have also been implemented and tested for the FP platform. TABLE 1 summarizes some of these developments. Despite its simplicity, alternating projection remains an effective algorithm for phase retrieval. More advanced optimization strategies for ptychographic phase retrieval have been discussed[67] in a wide-ranging survey covering conjugate gradient, Newton-type second-order optimization, set projection approaches and the relaxed average alternating reflections method. Reference[62] is a comprehensive review of first- and second-order optimization approaches for FP datasets. It was shown that the second-order Gauss–Newton method with amplitude-based cost function gave the best results in general. In practice, if the data are reasonably clean, the phase retrieval process is typically well conditioned and any optimization technique may be used — from alternating projection to advanced non-linear approaches.

Another trend of algorithm development related to FP is the employment of data-driven approaches or neural networks in the imaging and reconstruction process. These developments can be categorized into four groups. The first group focuses on inferring the high-resolution intensity and/or the phase images from the low-resolution FP measurements[68–73]. For example, deep neural networks have been used to produce high-resolution images from FP raw measurements[68,73]. More recently, a Bayesian network has been used to output both the high-resolution phase images and uncertainty maps of the predictions[71].

The second group focuses on incorporating the physical model into the design of the network[74–78]. The training of the network can jointly optimize the physical parameters used in the acquisition, such as the coded illumination pattern of the LED array. For instance, a neural network has been used to optimize the LED array illumination, in order to highlight important sample features for classification tasks[77]. In another example, a framework was used to create interpretable, context-specific LED source patterns for FP illumination[78].

The third group of developments is to model the forward FP imaging problem using neural networks and perform optimization via a network training process[79–82]. This process is also termed automatic differentiation or algorithmic differentiation, where derivatives can be efficiently evaluated based on the forward model[83]. For FP, the complex object can be treated as the learnable weights of a convolutional layer. The output of the network can be modelled as the loss function that one aims to minimize. Different solvers and acceleration strategies from machine learning libraries can then be adopted in the optimization process.

Finally, the recovered image of FP can be passed through a neural network for further improvement. For example, virtual brightfield and fluorescence staining can be performed on FP recovered images without paired training data[84]. Coherent artefacts of FP reconstructions can also be reduced in this unsupervised image translation process.

***New hardware implementations.*** The use of an LED array is not the only approach for implementing FP[6], and various hardware-based FP schemes have been reported. We discuss representative examples in the following.

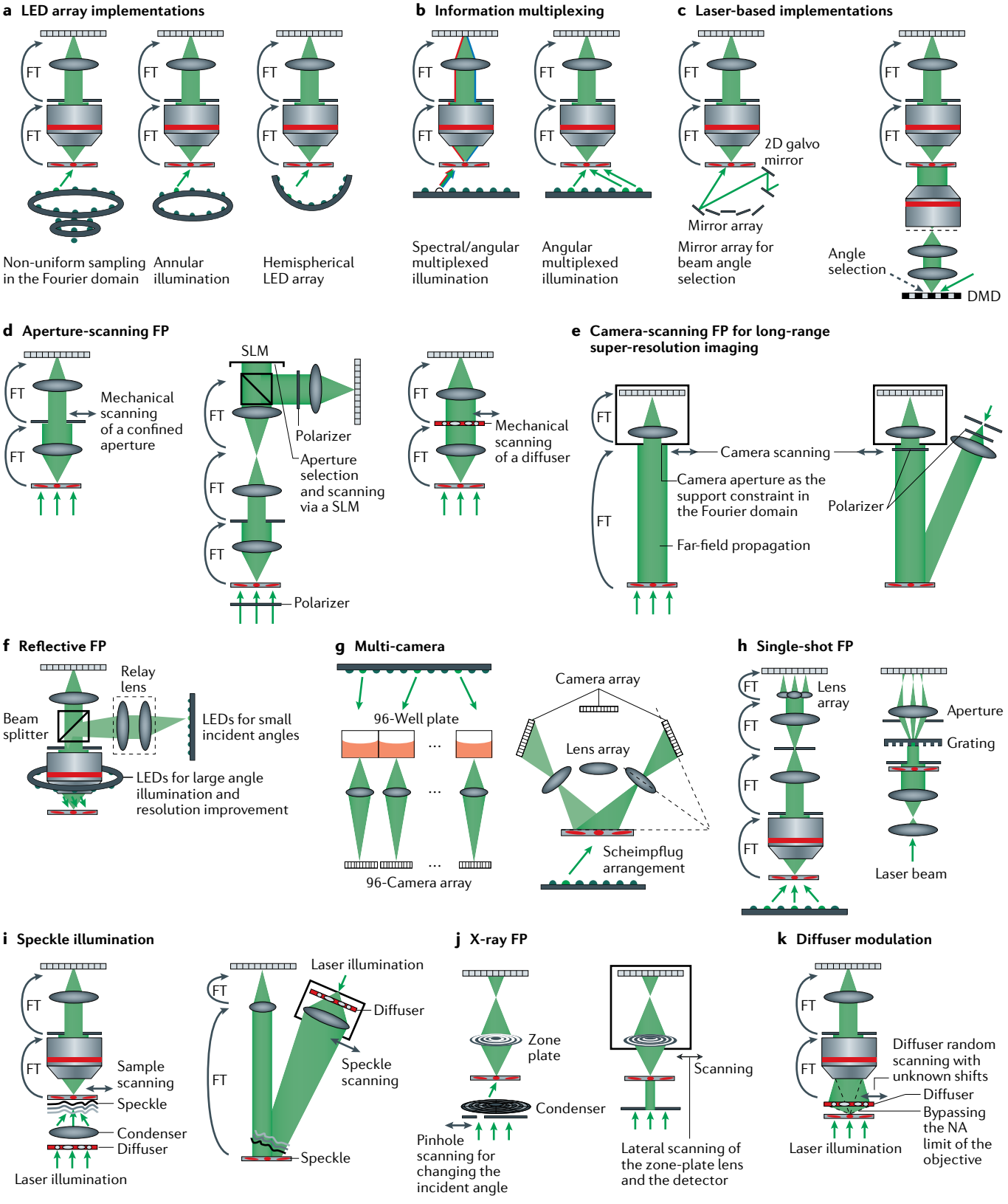


The first example is aperture-scanning FP, in which the specimen is illuminated by a fixed plane wave and an aperture is placed at the Fourier plane of the optical system (FIG. 2d). By translating the aperture to different lateral positions in the Fourier plane, images can be captured and synthesized in the Fourier domain to perform FP reconstruction. The key innovation of this scheme is that the recovered image does not depend on how the complex wavefront enters the sample but, rather, how it exits. Thus, the sample thickness becomes irrelevant during reconstruction. One can backpropagate the exit wave to any plane along the optical axis for 3D imaging.

◀ Fig. 2 | **Implementations of Fourier ptychography. a** | Fourier ptychography (FP) implementations using LED arrays, including non-uniform sampling in the Fourier space[42], annular illumination for phase imaging[56] and illumination via a hemispherical LED array[36–38]. **b** | Information multiplexing for FP, in which multiple LEDs with different colours[43,45,46] and/or different incident angles[43,44,47] can be turned on at the same time for sample illumination. Properly chosen multiplexed angles can shorten the acquisition time for in vitro imaging[47]. **c** | FP via laser-based illuminations, including the use of a mirror array[50] and a digital micromirror device (DMD)[49] for rapidly changing the incident angle. **d** | Aperture-scanning FP. An aperture[7,87,94] or a diffuser[86] can be scanned to different positions at the Fourier plane. The aperture-scanning process can also be performed using a spatial light modulator (SLM)[85] or a diffraction grating[88] without involving mechanical scanning. **e** | Camera-scanning FP. By placing the object at the far field, the lens aperture naturally serves as an aperture constraint at the Fourier plane. By scanning the lens and the detector to different lateral positions, a super-resolution complex object image can be synthesized in the Fourier plane[7,8,89]. **f** | Reflective FP, in which light is delivered through the epi-illumination path[90–92]. An LED ring array can be placed outside the objective for further resolution improvement[90,93]. **g** | Multi-camera scheme for parallel acquisition[96,97,119]. **h** | Single-shot FP using a lens array[98] and a grating[88,99]. **i** | A translated speckle pattern, that is, a coherent sum of different plane waves, can be used for sample illumination[101–105]. **j** | X-ray FP via pinhole scanning[9] and lens translation[9,107]. **k** | A diffuser at the detection path can be used to modulate the exit wavefront of the complex object, in effect, bypassing the numerical aperture (NA) limit of the objective[113,114]. This scheme can address the 2D model limitation of FP and image 3D thick samples. FT, Fourier transform.

This scheme was first demonstrated using a mechanical stage to translate the aperture[7] (FIG. 2d, left panel). Later, a spatial light modulator was adopted for digital scanning[85] (FIG. 2d, centre panel). Other related developments include scanning a diffuser at the Fourier plane[86] (FIG. 2d, right panel), dual-wavelength implementation for phase unwrapping[87] and single-shot implementation using a grating[88].

The second example of a hardware-based scheme is camera-scanning FP for long-range super-resolution imaging[7,8,89]. In this approach (FIG. 2e), the specimen is placed at the far field and a photographic camera is used to capture images. Far-field propagation of the light waves corresponds to the operation of a Fourier transform. As such, the lens aperture placed at the far field serves as a confined aperture constraint in the Fourier domain. By moving the entire camera, one can capture multiple images corresponding to different circular apertures at the Fourier plane. These images can then be synthesized to form a super-resolution exit wavefront of the object. The final resolution is not determined by the lens aperture. Instead, it is determined by how far one can translate the camera. The scheme has been demonstrated with a transmission mode[7] (FIG. 2e, left panel) and later in a reflection mode for imaging diffused objects[8] (FIG. 2e, right panel).

The third example is reflective implementations[87,90–95] (FIG. 2f). Angle-varied illumination in the original FP set-up can be implemented in the epi-illumination arm in a reflection mode. An LED ring can be mounted outside the objective lens for sample illumination with large incident angles[90,93]. Other related developments include an off-axis configuration with angle-varied illumination[95] and the implementation of aperture-scanning FP in a reflection mode[94].

The fourth example is multi-camera implementation. A high-throughput screening system has been demonstrated using 96 repeating low-cost microscope units[96] (FIG. 2g, left panel). This platform can image the entire 96-well plate at a rate of 0.7 frames per second. In another configuration, a camera array was arranged according to the Scheimpflug principle[97] (FIG. 2g, right panel). Using multiple cameras in an FP platform has the potential to substantially increase the imaging throughput.

The fifth example is the single-shot FP implementation (FIG. 2h). In one reported set-up, a lens array has been placed at the Fourier plane of the objective lens and multiple object images are collected in a single shot using the angular multiplexing strategy[98] (FIG. 2h, left panel). Similarly, single-shot implementations can be achieved via a diffraction grating[88,99] (FIG. 2h, right panel) and colour-multiplexed annular illumination[43]. These different implementations essentially trade off the imaging FOV to achieve the single-shot capability.

The sixth example is a speckle illumination scheme (FIG. 2i). The speckle pattern on the specimen can be considered as an amalgamation of localized phase gradients, each of which approximates a plane wave with different angle of incidence. Laterally translating the speckle or the object changes the phase gradient that illuminates a given region of the specimen, similar to the original angle-varied illumination concept in FP. One key distinction is that the translated speckle illumination scheme can be used for both coherent and incoherent imaging. When it is implemented for incoherent fluorescence imaging, it is conceptually similar to structured illumination microscopy[100]. The final achievable resolution is jointly determined by the NA of the objective lens and the feature size of the speckle pattern. This scheme has been demonstrated for fluorescence imaging beyond the diffraction limit of the objective lens[101]. To further improve the performance, a high-NA condenser lens can be used to generate speckle patterns and a low-NA objective lens can be used to acquire the fluorescence images[102]. By using this strategy, a 4-fold resolution gain was achieved for a fluorescence microscope set-up and a 13-fold resolution gain was achieved for imaging through a low-pass diffusing layer. More recently, this concept has been extended to coherent imaging systems[103,104]. Using a 0.12-NA objective lens for image acquisition, a synthetic NA of 0.85 has been achieved for the reconstructed images[103] (FIG. 2i, left panel). Interestingly, the translated speckle scheme can also be used for long-range super-resolution imaging. As shown in the right panel of FIG. 2i, a translated speckle pattern is projected on the remote objects and a regular photographic lens is used for image acquisition. Based on the modulation process of the projected speckle pattern, the high-resolution object information can be encoded into the captured images — information that would otherwise be inaccessible. This scheme has been validated for both coherent and incoherent long-range imaging settings[103,105]. Up to sevenfold resolution improvement has been experimentally demonstrated[103].

Finally, the FP method can be implemented in coherent X-ray microscopy for super-resolution nanoscale imaging[9,106–108]. FIGURE 2j shows two representative schemes of X-ray FP. The first one employs a scanning pinhole to select different illumination angles from the different subfields of a condenser[9]. In this scheme, the resolution is limited by the combined NA of the condenser and objective. The second scheme is conceptually

similar to the camera-scanning implementation shown in FIG. 2e. In it, both the objective lens and the detector are scanned through the diffraction beam[9,106,107], thereby avoiding the complexity of maintaining constant illumination while changing the incident angle. The scan range extends the NA of the objective lens, effectively forming a synthetic lens with an NA larger than any available X-ray optics. The set-up achieves a resolution that is limited by the scan range and exhibits unexpectedly high dose efficiency compared with the regular transmission X-ray microscopy[9]. More recently, a Fourier synthesis strategy similar to FP has been implemented in a Bragg coherent X-ray diffraction imaging experiment[108]. Resolution improvement in 3D has been demonstrated for crystalline materials[108].

***Addressing the model limitation.*** In the forward imaging model of FP discussed in BOX 1, the complex object $O(x, y)$ is multiplied with the incident plane wave $e^{ik_{xi}x}e^{ik_{yi}y}$ before passing through the low-pass microscope system. This multiplication process assumes that the object section is infinitesimally thin. For any practical object, tilting the illumination plane wave would also change the spectrum of the object and not only shift it in the Fourier space. In a wave optics picture, tilting the illumination would rock the Ewald sphere around the origin. The objective lens lets through a solid angle of scattered beams that subsequently form an image at the detector plane. As such, each captured image corresponds to a spherical cap of the Ewald sphere in the Fourier space. These spherical caps do not span a single 2D plane in the Fourier domain. There are two strategies to address this problem.

The first strategy is to adopt a better forward imaging model by considering the 3D nature of the object. Multi-slice modelling, originally proposed for electron microscopy[109], is one example of this strategy, and it has found great success in real-space ptychography[28,110]. In this approach, the 3D object is represented by a series of 2D thin slices separated by a certain distance. The incident wave from the light source multiplies with the first layer to form an exit wave, which is propagated to the second layer, where it forms a new incident wave. This process goes through the whole specimen. The use of multi-slice modelling to image 3D specimens has been demonstrated using an FP microscope set-up[15,111]. Its advantage is that it does not make any weak or single-scattering approximations. The serial scattering from each slice accounts for the multiple scattering effect in the forward direction. Backscattered light has not been considered in existing implementations.

Another approach to account for the 3D nature of the object is diffraction tomography. In this approach, the object is represented by 3D scattering potential. Under the first-order Born or Rytov approximations, the captured images in an FP microscope can be used to update the corresponding spherical cap region of the 3D scattering potential in the Fourier domain. Beyond a first implementation of diffraction tomography with FP[10], a high-throughput FP diffraction tomography platform has been demonstrated using darkfield measurements with large illumination NA[11].

Despite these successes, isotropic resolution remains elusive for these two methods, owing to the missing cone problem. Specifically, the 3D coherent transfer function of an imaging system under single or weak scattering approximations has a doughnut shape owing to the limited aperture. The missing frequency near the origin along the $k_z$ direction in the Fourier domain results in a loss of spatial resolution along the $z$ axis. It has been shown that multiple scattering can mitigate the missing cone problem and, hence, the multi-slice model may perform better in principle[112]. Computationally filling in the missing cone via some priors is also a possible strategy for both approaches. Similarly, a better forward imaging model can bring in reconstruction with higher fidelity. Thus, future developments include a multi-slice model considering backward scattering and a diffraction tomography model considering multiple scattering. A possible challenge for both approaches is the high computational demand in the reconstruction process, which can often take hours or days to recover the full 3D volume.

The second strategy for addressing the 2D modelling problem in FP is to keep the illumination angle fixed and perform modulation at the detection path. In this case, the recovered complex image represents the exit wavefront of the object. The thickness of the object is irrelevant in the modelling. Aperture-scanning and camera-scanning FP are two examples of this strategy (FIG. 2d,e). However, for aperture-scanning FP, the achievable resolution is limited by the NA of the first objective lens. This resolution limitation has been addressed by translating a thin diffuser in between the specimen and the objective lens[113,114] (FIG. 2k). In this approach, the diffuser serves as a thin scattering lens for light wave modulation. The multiplication process between the object and the tilted plane wave in the original FP set-up becomes the multiplication between the object exit wavefront and the thin diffuser profile. Enabled by this multiplication process, the otherwise inaccessible high-resolution object information can be encoded into the captured images. A 4.5-fold resolution improvement over the diffraction limit of the objective lens has been demonstrated using this approach[113]. It was also shown that a fourfold resolution gain can be achieved with as few as ~30 raw images.

## Applications of Fourier ptychography

***Quantitative phase imaging in 2D and 3D.*** In biomedical imaging, unlabelled specimens are often inherently transparent. Thus, phase provides a complementary contrast mechanism to reveal the detailed structures that are otherwise invisible in brightfield images. Over the past two decades, quantitative phase imaging (QPI) has emerged as a valuable tool for investigating various weakly scattering and weakly absorbing specimens.

The QPI capability of FP has been validated by comparing the recovered phase to the results of phase-shifting digital holography[115]. QPI applications on a variety of biological samples have emerged since then. FIGURE 3a shows the FP-recovered phase image of a blood smear[115,116], from which phase-gradient and gradient-magnitude images can be generated post-measurement. FIGURE 3b shows the recovered phase

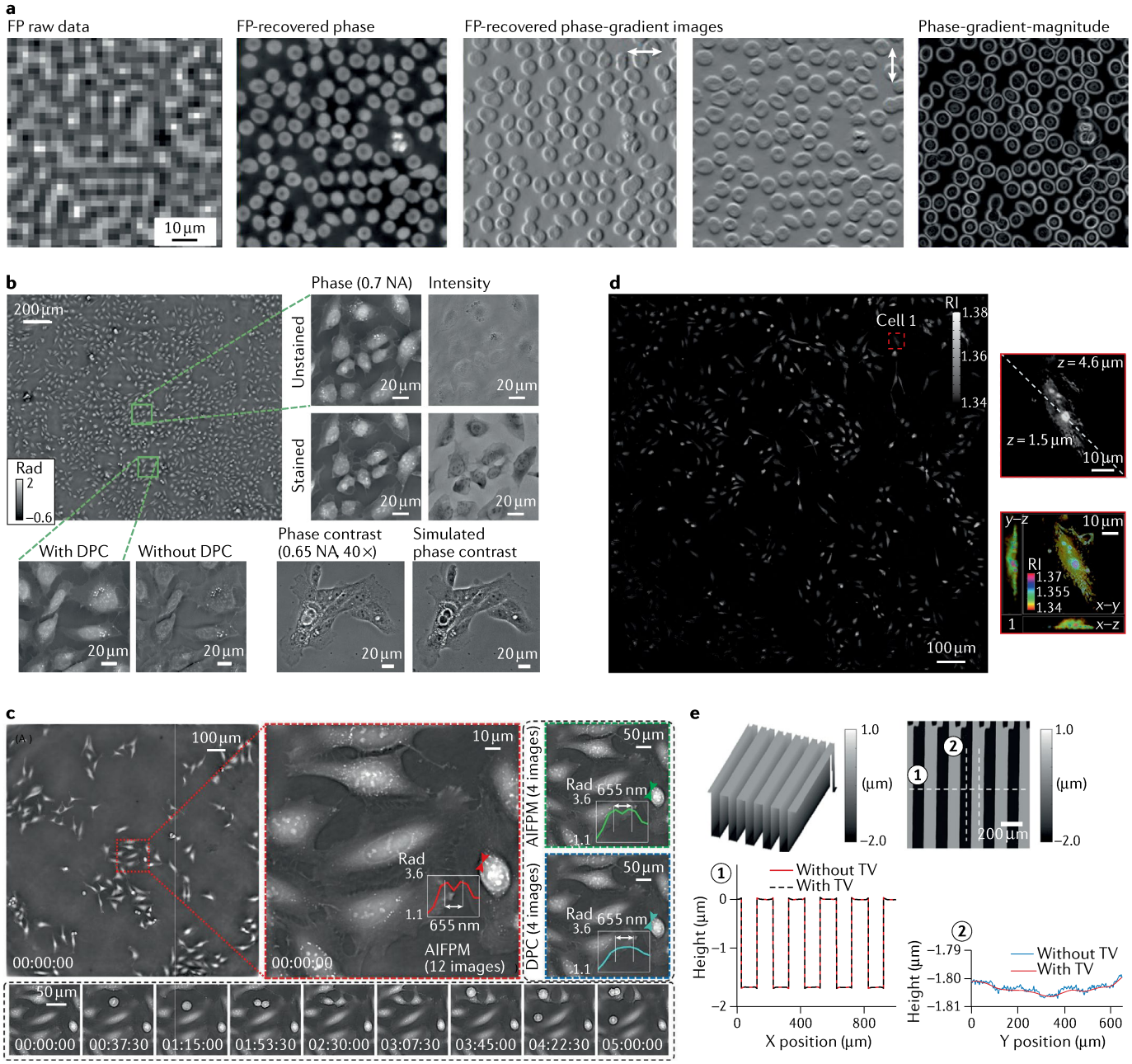


Fig. 3 | **Quantitative phase imaging in 2D and 3D. a** | Quantitative phase imaging (QPI) of a blood smear[115,116]. The recovered phase can be further used to generate phase-gradient and phase-gradient-magnitude images. **b** | Recovered phase images via the in vitro FP implementation, in which the initial phase is generated by differential-phase-contrast (DPC) imaging. **c** | QPI via annular illumination Fourier ptychographic microscopy (AIFPM), in which low-frequency phase information can be effectively converted into FP intensity measurements. Cell mitosis and apoptosis events can be captured at a frame rate of 25 Hz. **d** | Fourier ptychographic diffraction tomography, in which the 3D refractive index (RI) of a cell culture is recovered from FP intensity measurements. A 390-nm lateral resolution and 899-nm axial resolution was achieved across a 10× field of view of 1.77 $mm^2$. **e** | Topographic map of a 3D surface via FP phase imaging, in which two wavelengths are employed to address the phase wrapping problem. FP, Fourier ptychography; NA, numerical aperture; TV, total variation denoising. Part **a** adapted with permission from REF.[116], IEEE. Part **b** adapted with permission from REF.[47], OSA. Part **c** adapted from REF.[56], CC BY 4.0. Part **d** adapted from REF.[11], CC BY 4.0. Part **e** adapted with permission from REF.[87], OSA.

images of live HeLa cell culture using the in vitro FP platform[47]. Similarly, FIG. 3c shows the high-speed QPI results of live HeLa cell culture using the annular illumination scheme[56], in which four images corresponding to four annular illumination angles were acquired and used for FP reconstructions.

QPI via FP also finds applications in 3D microscopy. The refractive index distribution of a biological sample can be used as intrinsic imaging contrast for label-free and quantitative bioimaging. Traditional diffraction tomography requires an interferometric set-up to measure the 2D holograms at each illumination angle.

FP can be integrated with the diffraction tomography framework to recover 3D scattering potential from intensity-only measurements[10]. FIGURE 3d shows the recovered 3D refractive index distribution of live HeLa cell culture using the Fourier ptychographic diffraction tomography approach[11].

Another application of QPI is optical metrology, in which topographic maps of a 3D surface can be generated by measuring spatially varying phase retardation. FIGURE 3e shows the recovered topographic map using aperture-scanning FP under the reflection mode[87]. To address the phase wrapping problem, dual-wavelength reconstruction was employed to eliminate the phase ambiguity. The line traces in FIG. 3e show a 1.8-μm height difference on a topographic surface, with a measurement error of a few nanometres.

***Digital pathology and cytometry.*** Conventional microscopes require constant readjustment of the axial stage to keep the sample in focus when the FOV is moved. FP addresses this drawback by using a digital refocusing process, in which the sample defocus is corrected for by a phase factor that is introduced in the objective's pupil function. Using this correction, FP can extend the depth of field by two orders of magnitude compared with a conventional microscope with a similar NA[4]. FP can also be used to recover an image that is all in focus by digitally refocusing many small segments of the entire image, which are then stitched together.

The combination of wide FOV, high resolution and the capability of digital refocusing post-measurement makes FP a promising candidate for digital pathology, in which digital images of stained histology slides are acquired and used for diagnostic purposes. The phase information recovered from FP provides information about the local scattering and reduced scattering coefficients of the sample. This information may be useful for pathology diagnosis and single-cell analysis[117] (FIG. 4a). One challenge of adopting FP for digital pathology is the coherent imaging nature of the technique. The recovered FP image may contain coherent artefacts that reduce the colour accuracy compared with the regular incoherent images. It is possible to apply unsupervised image-to-image translation to convert the FP constructions into the style of regular incoherent microscopy[84]. FIGURE 4b shows the fluorescence image obtained by virtually staining the FP reconstruction. The appearance of the network output is similar to those captured using regular incoherent microscope platforms.

FP also finds applications in high-throughput cytometry. For example, circulating tumour cells are a candidate biomarker that may enable prognosis and prediction in metastatic disease. FIGURE 4c shows the full FOV colour image of the entire microfilter containing captured tumour cells[118]. Similarly, cell analysis can also be performed on the FP-recovered high-content images for disease diagnoses. FIGURE 4d shows the recovered phase image of a blood smear using a high-NA FP system[30]. The phase information can be used to identify, for example, malaria-infected cells[35]. It is also possible to optimize the illumination pattern to improve the accuracy of malaria-infected cell classification[76]. Another example is high-content screening using multiwell plates[96,119]. FIGURE 4e shows a parallel microscopy system that can simultaneously image all wells on a 96-well plate via FP. The system can also perform fluorescence imaging at the native resolution of the 96 objectives.

***Aberration metrology.*** FP can correct optical aberrations through computational post-measurement processing[65]. An improved version of FP with a rigorous aberration model was proposed in 2019 (REF.[66]). Instead of recovering pupil function individually for each tile, it considers the field dependence across the entire FOV, in effect, reducing the degrees of freedom in the optimization process. This approach provides an effective tool for measuring aberrations of an optical system. FIGURE 5a shows the recovered complex objects and the pupils using this approach. The aberration metrology ability of FP also makes it suitable for settings in which optically reducing aberration is unattainable, such as in situ aberration correction for cellphone lenses[53], mouldless droplet lenses[120] and camera module lenses[54].

Once the optical system aberration has been determined, it can be applied to other imaging modalities using the same set-up. To this end, an approach termed 'coded-aperture-based correction of aberration obtained from overlapped Fourier coding and blur estimation' (CACAO-FB) has been reported[121]. In this approach, the system sequentially opens the sub-apertures on the pupil plane and acquires the corresponding intensity projections. Different pupil segments are stitched via FP and the recovered coherent transfer function is then used to deconvolve the coded aperture images under incoherent illumination. As shown in FIG. 5b, an in vivo retinal imaging experiment on a rhesus macaque was demonstrated using this approach. Similarly, FIG. 5c shows the recovered intensity, phase gradient and deconvolved fluorescence images of a multimodal imaging system[122], in which the recovered aberration by FP is used to deconvolve the fluorescence images.

***Surface inspection.*** FP in a reflective configuration can be used for surface inspection. FIGURE 5d demonstrates the use of a reflected FP set-up for examining a high-density integrated circuit of a smartphone[93]. In this set-up, a parabolic mirror is used to direct the beams towards the object at large incident angles. However, this set-up is only effective for single-layer surfaces owing to the wave-object multiplication process in the forward imaging model. To image a general 3D reflective object, an aperture-scanning FP[7] or diffuser modulation scheme[113] can be used to address the model limitation discussed above. FIGURE 5e shows the four recovered spectral channels of a 3D flip chip using a multispectral aperture-scanning FP set-up with computational aberration correction[94]. The large 3D micro-ball bump can be clearly seen in region 1 in FIG. 5e.

***Camera-scanning Fourier ptychography for long-range imaging and X-ray nanoscopy.*** The camera-scanning FP scheme[7] has applications in remote sensing, forensics and surveillance. FIGURE 5f shows a raw image and its

reconstruction using the camera-scanning FP scheme, with a sixfold resolution gain for the FP reconstructions compared with that set by the lens aperture[8]. The camera-scanning concept can also be adopted in an X-ray nanoscopy set-up. By translating the objective lens and the detector, one can bypass the diffraction limit of the zone-plate lens[9,106,107]. FIGURE 5g shows the recovered image of a silicon chip by X-ray FP. The Fourier ring

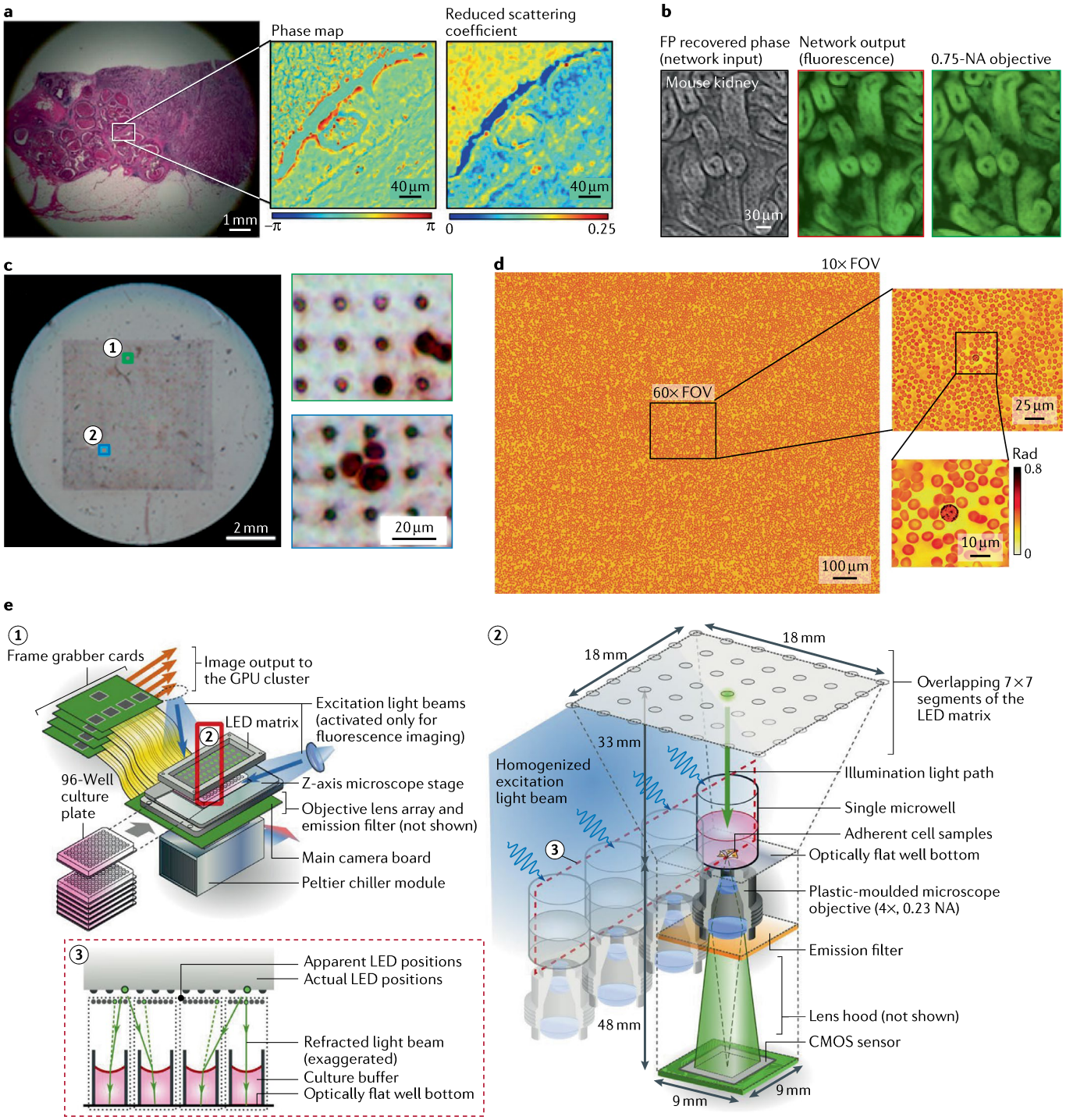


Fig. 4 | **Digital pathology and high-throughput cytometry via Fourier ptychography. a** | Fourier ptychography (FP) can generate wide-field-of-view (FOV) and high-resolution images of pathology slides[65,117]. The phase map shows the optical path length delays introduced by the specimen and the reduced scattering coefficient map quantifies how much light has been scattered by the specimen. **b** | Virtual colour and fluorescence staining of FP reconstructions via unsupervised image-to-image translation. **c** | Full FOV colour image of the entire microfilter containing captured tumour cells. Magnified regions indicate the level of detail of cell morphology that can be seen. **d** | High-resolution recovered phase of a blood smear for cell analysis. **e** | Parallel FP system that is capable of simultaneously imaging all wells on a 96-well plate. CMOS, complementary metal–oxide–semiconductor; GPU, graphics processing unit; NA, numerical aperture. Part **a** adapted with permission from REF.[65], OSA. Part **b** adapted with permission from REF.[84], OSA. Part **c** adapted from REF.[118], CC BY 3.0. Part **d** adapted from REF.[30], CC BY 4.0. Part **e** adapted from REF.[96], CC BY 4.0.

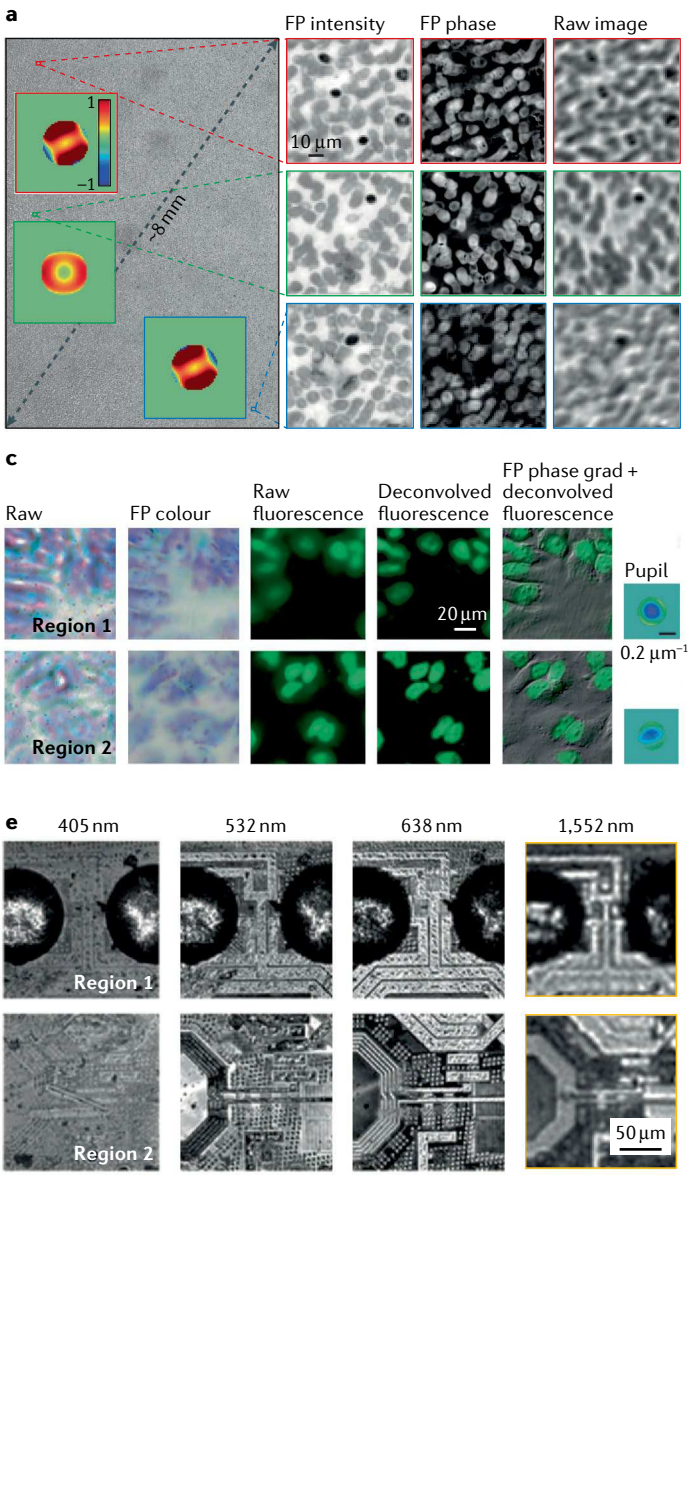


correlation between two independent scans was used to estimate the resolution to be 47 nm, significantly below the Rayleigh limit of 85 nm for the employed zone-plate objective[9].

## Outlook

Real-space ptychography has become an indispensable imaging modality in most X-ray synchrotron laboratories worldwide. We anticipate that FP, currently in its early stage, will continue to grow and expand in applications. We identified the following areas for potential further developments of the FP approach.

- Algorithms for blind FP reconstruction. Current challenging cases for blind FP reconstruction include specimens with many phase wraps (such as rough reflected surfaces), optical systems with severe unknown aberrations, light sources with low spatial and temporal coherence, measurements with

◀ Fig. 5 | **Aberration metrology, surface inspection, long-range imaging and X-ray nanoscopy via Fourier ptychography. a** | Aberration recovery using a full-field model in Fourier ptychography (FP). The three colour maps show the recovered pupil aberrations at three locations of the field of view. The recovered FP intensity, FP phase and the raw image at these three locations are shown in columns 2–4. **b** | In vivo eye imaging via CACAO-FB (coded-aperture-based correction of aberration obtained from overlapped Fourier coding and blur estimation). **c** | A multimodal imaging system, in which pupil aberrations at three different locations can be recovered by FP (column 6). The recovered pupils are then used to deconvolve the raw fluorescence images in column 3 to generate the corrected images in column 4. **d** | Super-resolution surface inspection of a circuit board via reflected FP. A synthetic numerical aperture (NA) of 1.06 is achieved using a 10×, 0.28-NA objective. **e** | Multispectral inspection of a silicon chip for fault detection via aperture-scanning FP. **f** | Long-range super-resolution imaging of a fingerprint via camera-scanning FP. **g** | Super-resolution image of a silicon chip via X-ray FP. The resolution is estimated to be 47 nm via the 1-bit criterion of Fourier ring correlation (FRC), that is, the intersection between the red curve and the dashed line. It is better than the Rayleigh resolution limit (RRL), marked by the dotted line. PSF, point spread function. Part **a** adapted from REF.[66], CC BY 4.0. Part **b** adapted with permission from REF.[121], OSA. Part **c** adapted with permission from REF.[122], OSA. Part **d** adapted with permission from REF.[93], OSA. Part **e** adapted with permission from REF.[94], OSA. Part **f** adapted with permission from REF.[8], AAAS. Part **g** adapted from REF.[9], CC BY 4.0.

interference fringe or other artefacts, and combinations of the above conditions. There have been attempts to convert the non-convex phase retrieval problem into a convex optimization problem. One prominent example is PhaseLift[123], which has been implemented in an FP setting[124]. In this approach, convex relaxation is needed to replace the rank constraint by a norm. For certain phase retrieval algorithms, it has been shown that the conditions that guarantee the correspondence between the non-convex problem and its convex relaxation are also sufficient to guarantee that the non-convex problem does not have local minima[125]. Therefore, recasting to convex relaxations may not necessarily give a better result compared with the non-convex ones. The developments of memory-efficient non-convex tools for handling these challenging cases are highly desired for the development of both FP and real-space ptychography.

- Implementations of FP in the EUV regime. The adoption of 13.5-nm EUV lithography has become a standard for manufacturing next-generation silicon chips. Identifying defects in an EUV mask is a challenging task and the related tools are among the most expensive in semiconductor fabrication facilities. It is also important to perform the inspection at the same 13.5-nm wavelength because defects are often wavelength-sensitive. Early development has demonstrated the use of angle-varied illumination to improve the resolution[95]. We envision that the lens translation strategy in X-ray FP could also be implemented for EUV light.
- FP for chemical imaging. Infrared wavelengths contain vibration modes of many molecular bonds. The higher wavenumber region is associated with stretching vibrations such as S–H, C–H, N–H and O–H; the lower wavenumber regions typically correspond to bending and carbon skeleton fingerprint vibrations. Implementing FP in these regions could lead to important applications in chemical imaging. Theoretical analysis has also shown the potential of applying FP for coherent anti-Stokes Raman scattering[126]. If successful, it could be an efficient approach for imaging thin tissue sections on specific Raman vibration transitions.
- FP for electron microscopy. The existing tilted series method in electron microscopy acquires images under angle-varied illuminations. However, it performs image reconstruction using linear restoring filters[32,33]. The iterative phase retrieval process in FP can be employed in tilted series reconstruction for 2D thin specimens. Fourier ptychographic diffraction tomography[10,11] or multi-slice modelling[15,111,112] can be used to handle 3D specimens.
- FP for education. The concept of FP can help students understand the basics of Fourier optics, including coherent transfer function, NA, pupil aberration and the Ewald sphere. The FP approach has become a sub-chapter in Joseph Goodman's textbook *Introduction to Fourier Optics* (4th edition)[127]. We envision the development of an FP microscope to be part of an optics lab course.
- Other applications. Many FP applications remain to be seen. To name a few, the aberration metrology capability[65,66,128] can be used to characterize the lens profile and the related optical transfer function; the high-throughput 96-camera platform[96] can be used for drug screening; the QPI capability in two dimensions and three dimensions can be used to detect bloodborne and waterborne pathogens; sample rotation can be integrated with the transmission X-ray FP for 3D nanoscopy; and diffraction tomography can be integrated with angle-varied illumination for imaging diffused reflective objects.

## Code availability

Example Fourier ptychography codes and datasets are available at https://github.com/SmartImagingLabUConn/Fourier-Ptychography

Published online: 10 February 2021


1. Lohmann, A. W., Dorsch, R. G., Mendlovic, D., Zalevsky, Z. & Ferreira, C. Space–bandwidth product of optical signals and systems. *JOSA A* **13**, 470–473 (1996).
2. McConnell, G. et al. A novel optical microscope for imaging large embryos and tissue volumes with sub-cellular resolution throughout. *eLife* **5**, e18659 (2016).
3. Fan, J. et al. Video-rate imaging of biological dynamics at centimetre scale and micrometre resolution. *Nat. Photonics* **13**, 809–816 (2019).
4. Zheng, G., Horstmeyer, R. & Yang, C. Wide-field, high-resolution Fourier ptychographic microscopy. *Nat. Photonics* **7**, 739–745 (2013).
5. Zheng, G., Kolner, C. & Yang, C. Microscopy refocusing and dark-field imaging by using a simple LED array. *Opt. Lett.* **36**, 3987–3989 (2011).
6. Zheng, G., Ou, X., Horstmeyer, R., Chung, J. & Yang, C. Fourier ptychographic microscopy: A gigapixel superscope for biomedicine. *Opt. Photonics News* **25**, 26–33 (2014).
7. Dong, S. et al. Aperture-scanning Fourier ptychography for 3D refocusing and super-resolution macroscopic imaging. *Opt. Express* **22**, 13586–13599 (2014).
8. Holloway, J., Wu, Y., Sharma, M. K., Cossairt, O. & Veeraraghavan, A. SAVI: Synthetic apertures for long-range, subdiffraction-limited visible imaging using Fourier ptychography. *Sci. Adv.* **3**, e1602564 (2017).
9. Wakonig, K. et al. X-ray Fourier ptychography. *Sci. Adv.* **5**, eaav0282 (2019).
10. Horstmeyer, R., Chung, J., Ou, X., Zheng, G. & Yang, C. Diffraction tomography with Fourier ptychography. *Optica* **3**, 827–835 (2016).
11. Zuo, C., Sun, J., Li, J., Asundi, A. & Chen, Q. Wide-field high-resolution 3D microscopy with Fourier ptychographic diffraction tomography. *Opt. Lasers Eng.* **128**, 106003 (2020).
12. Ryle, M. & Hewish, A. The synthesis of large radio telescopes. *Mon. Not. R. Astron. Soc.* **120**, 220–230 (1960).
13. Gerchberg, R. W. A practical algorithm for the determination of phase from image and

diffraction plane pictures. *Optik* **35**, 237–246 (1972).
14. Fienup, J. R. Phase retrieval algorithms: a comparison. *Appl. Opt.* **21**, 2758–2769 (1982).
15. Li, P., Batey, D. J., Edo, T. B. & Rodenburg, J. M. Separation of three-dimensional scattering effects in tilt-series Fourier ptychography. *Ultramicroscopy* **158**, 1–7 (2015).
16. Hoppe, W. & Strube, G. Diffraction in inhomogeneous primary wave fields. 2. Optical experiments for phase determination of lattice interferences. *Acta Crystallogr. A* **25**, 502–507 (1969).
17. Faulkner, H. M. L. & Rodenburg, J. Movable aperture lensless transmission microscopy: a novel phase retrieval algorithm. *Phys. Rev. Lett.* **93**, 023903 (2004).
18. Guizar-Sicairos, M. & Fienup, J. R. Phase retrieval with transverse translation diversity: a nonlinear optimization approach. *Opt. Express* **16**, 7264–7278 (2008).
19. Thibault, P., Dierolf, M., Bunk, O., Menzel, A. & Pfeiffer, F. Probe retrieval in ptychographic coherent diffractive imaging. *Ultramicroscopy* **109**, 338–343 (2009).
20. Maiden, A. M. & Rodenburg, J. M. An improved ptychographical phase retrieval algorithm for diffractive imaging. *Ultramicroscopy* **109**, 1256–1262 (2009).
21. Dierolf, M. et al. Ptychographic X-ray computed tomography at the nanoscale. *Nature* **467**, 436–439 (2010).
22. Maiden, A. M., Humphry, M. J., Zhang, F. & Rodenburg, J. M. Superresolution imaging via ptychography. *JOSA A* **28**, 604–612 (2011).
23. Thibault, P. & Menzel, A. Reconstructing state mixtures from diffraction measurements. *Nature* **494**, 68–71 (2013).
24. Batey, D. J., Claus, D. & Rodenburg, J. M. Information multiplexing in ptychography. *Ultramicroscopy* **138**, 13–21 (2014).
25. Rodenburg, J. & Maiden, A. in *Springer Handbook of Microscopy* Ch. 17 (eds Hawkes, P. W. & Spence, J. C. H.) 819–904 (Springer, 2019).
26. Horstmeyer, R. & Yang, C. A phase space model of Fourier ptychographic microscopy. *Opt. Express* **22**, 338–358 (2014).
27. Li, P. & Maiden, A. Lensless LED matrix ptychographic microscope: problems and solutions. *Appl. Opt.* **57**, 1800–1806 (2018).
28. Maiden, A. M., Humphry, M. J. & Rodenburg, J. Ptychographic transmission microscopy in three dimensions using a multi-slice approach. *JOSA A* **29**, 1606–1614 (2012).
29. Zhang, F. et al. Translation position determination in ptychographic coherent diffraction imaging. *Opt. Express* **21**, 13592–13606 (2013).
30. Sun, J., Zuo, C., Zhang, L. & Chen, Q. Resolution-enhanced Fourier ptychographic microscopy based on high-numerical-aperture illuminations. *Sci. Rep.* **7**, 1187 (2017).
31. Song, P. et al. Super-resolved multispectral lensless microscopy via angle-tilted, wavelength-multiplexed ptychographic modulation. *Opt. Lett.* **45**, 3486–3489 (2020).
32. Kirkland, A., Saxton, W., Chau, K.-L., Tsuno, K. & Kawasaki, M. Super-resolution by aperture synthesis: tilt series reconstruction in CTEM. *Ultramicroscopy* **57**, 355–374 (1995).
33. Haigh, S. J., Sawada, H. & Kirkland, A. I. Atomic structure imaging beyond conventional resolution limits in the transmission electron microscope. *Phys. Rev. Lett.* **103**, 126101 (2009).
34. Horstmeyer, R., Heintzmann, R., Popescu, G., Waller, L. & Yang, C. Standardizing the resolution claims for coherent microscopy. *Nat. Photonics* **10**, 68–71 (2016).
35. Ou, X., Horstmeyer, R., Zheng, G. & Yang, C. High numerical aperture Fourier ptychography: principle, implementation and characterization. *Opt. Express* **23**, 3472–3491 (2015).
36. Sen, S., Ahmed, I., Aljubran, B., Bernussi, A. A. & de Peralta, L. G. Fourier ptychographic microscopy using an infrared-emitting hemispherical digital condenser. *Appl. Opt.* **55**, 6421–6427 (2016).
37. Pan, A. et al. Subwavelength resolution Fourier ptychography with hemispherical digital condensers. *Opt. Express* **26**, 23119–23131 (2018).
38. Phillips, Z. F., Eckert, R. & Waller, L. in *Imaging Systems and Applications* IW4E.5 (Optical Society of America, 2017).
39. Bian, L. et al. Content adaptive illumination for Fourier ptychography. *Opt. Lett.* **39**, 6648–6651 (2014).
40. Zhang, Y., Jiang, W., Tian, L., Waller, L. & Dai, Q. Self-learning based Fourier ptychographic microscopy. *Opt. Express* **23**, 18471–18486 (2015).
41. Li, S., Wang, Y., Wu, W. & Liang, Y. Predictive searching algorithm for Fourier ptychography. *J. Opt.* **19**, 125605 (2017).
42. Guo, K., Dong, S., Nanda, P. & Zheng, G. Optimization of sampling pattern and the design of Fourier ptychographic illuminator. *Opt. Express* **23**, 6171–6180 (2015).
43. Sun, J., Chen, Q., Zhang, J., Fan, Y. & Zuo, C. Single-shot quantitative phase microscopy based on color-multiplexed Fourier ptychography. *Opt. Lett.* **43**, 3365–3368 (2018).
44. Tian, L., Li, X., Ramchandran, K. & Waller, L. Multiplexed coded illumination for Fourier Ptychography with an LED array microscope. *Biomed. Opt. Express* **5**, 2376–2389 (2014).
45. Dong, S., Shiradkar, R., Nanda, P. & Zheng, G. Spectral multiplexing and coherent-state decomposition in Fourier ptychographic imaging. *Biomed. Opt. Express* **5**, 1757–1767 (2014).
46. Zhou, Y. et al. Fourier ptychographic microscopy using wavelength multiplexing. *J. Biomed. Opt.* **22**, 066006 (2017).
47. Tian, L. et al. Computational illumination for high-speed in vitro Fourier ptychographic microscopy. *Optica* **2**, 904–911 (2015).
48. Tian, L. & Waller, L. Quantitative differential phase contrast imaging in an LED array microscope. *Opt. Express* **23**, 11394–11403 (2015).
49. Kuang, C. et al. Digital micromirror device-based laser-illumination Fourier ptychographic microscopy. *Opt. Express* **23**, 26999–27010 (2015).
50. Chung, J., Lu, H., Ou, X., Zhou, H. & Yang, C. Wide-field Fourier ptychographic microscopy using laser illumination source. *Biomed. Opt. Express* **7**, 4787–4802 (2016).
51. Tao, X. et al. Tunable-illumination for laser Fourier ptychographic microscopy based on a background noise-reducing system. *Opt. Commun.* **468**, 125764 (2020).
52. Aidukas, T., Konda, P. C., Harvey, A. R., Padgett, M. J. & Moreau, P.-A. Phase and amplitude imaging with quantum correlations through Fourier ptychography. *Sci. Rep.* **9**, 10445 (2019).
53. Dong, S., Guo, K., Nanda, P., Shiradkar, R. & Zheng, G. FPscope: a field-portable high-resolution microscope using a cellphone lens. *Biomed. Opt. Express* **5**, 3305–3310 (2014).
54. Aidukas, T., Eckert, R., Harvey, A. R., Waller, L. & Konda, P. C. Low-cost, sub-micron resolution, wide-field computational microscopy using opensource hardware. *Sci. Rep.* **9**, 7457 (2019).
55. Guo, C. et al. OpenWSI: a low-cost, high-throughput whole slide imaging system via single-frame autofocusing and open-source hardware. *Opt. Lett.* **45**, 260–263 (2020).
56. Sun, J., Zuo, C., Zhang, J., Fan, Y. & Chen, Q. High-speed Fourier ptychographic microscopy based on programmable annular illuminations. *Sci. Rep.* **8**, 7669 (2018).
57. Bian, Z., Dong, S. & Zheng, G. Adaptive system correction for robust Fourier ptychographic imaging. *Opt. Express* **21**, 32400–32410 (2013).
58. Pan, A. et al. System calibration method for Fourier ptychographic microscopy. *J. Biomed. Opt.* **22**, 096005 (2017).
59. Sun, J., Chen, Q., Zhang, Y. & Zuo, C. Efficient positional misalignment correction method for Fourier ptychographic microscopy. *Biomed. Opt. Express* **7**, 1336–1350 (2016).
60. Eckert, R., Phillips, Z. F. & Waller, L. Efficient illumination angle self-calibration in Fourier ptychography. *Appl. Opt.* **57**, 5434–5442 (2018).
61. Zhou, A. et al. Fast and robust misalignment correction of Fourier ptychographic microscopy for full field of view reconstruction. *Opt. Express* **26**, 23661–23674 (2018).
62. Yeh, L.-H. et al. Experimental robustness of Fourier ptychography phase retrieval algorithms. *Opt. Express* **23**, 33214–33240 (2015).
63. Liu, J. et al. Stable and robust frequency domain position compensation strategy for Fourier ptychographic microscopy. *Opt. Express* **25**, 28053–28067 (2017).
64. Zheng, G., Ou, X., Horstmeyer, R. & Yang, C. Characterization of spatially varying aberrations for wide field-of-view microscopy. *Opt. Express* **21**, 15131–15143 (2013).
65. Ou, X., Zheng, G. & Yang, C. Embedded pupil function recovery for Fourier ptychographic microscopy. *Opt. Express* **22**, 4960–4972 (2014).
66. Song, P. et al. Full-field Fourier ptychography (FFP): Spatially varying pupil modeling and its application for rapid field-dependent aberration metrology. *APL Photonics* **4**, 050802 (2019).
67. Yang, C., Qian, J., Schirotzek, A., Maia, F. & Marchesini, S. Iterative algorithms for ptychographic phase retrieval. Preprint at https://arxiv.org/abs/1105.5628 (2011).
68. Nguyen, T., Xue, Y., Li, Y., Tian, L. & Nehmetallah, G. Deep learning approach for Fourier ptychography microscopy. *Opt. Express* **26**, 26470–26484 (2018).
69. Boominathan, L., Maniparambil, M., Gupta, H., Baburajan, R. & Mitra, K. Phase retrieval for Fourier Ptychography under varying amount of measurements. Preprint at https://arxiv.org/abs/1805.03593 (2018).
70. Kappeler, A., Ghosh, S., Holloway, J., Cossairt, O. & Katsaggelos, A. in *2017 IEEE International Conference on Image Processing (ICIP)* 1712–1716 (IEEE, 2017).
71. Xue, Y., Cheng, S., Li, Y. & Tian, L. Reliable deep-learning-based phase imaging with uncertainty quantification. *Optica* **6**, 618–629 (2019).
72. Shamshad, F., Abbas, F. & Ahmed, A. in *2019 IEEE International Conference on Acoustics, Speech and Signal Processing (ICASSP 2019)* 7720–7724 (IEEE, 2019).
73. Zhang, J., Xu, T., Shen, Z., Qiao, Y. & Zhang, Y. Fourier ptychographic microscopy reconstruction with multiscale deep residual network. *Opt. Express* **27**, 8612–8625 (2019).
74. Cheng, Y. F. et al. Illumination pattern design with deep learning for single-shot Fourier ptychographic microscopy. *Opt. Express* **27**, 644–656 (2019).
75. Kellman, M. R., Bostan, E., Repina, N. A. & Waller, L. Physics-based learned design: optimized coded-illumination for quantitative phase imaging. *IEEE Trans. Comput. Imaging* **5**, 344–353 (2019).
76. Muthumbi, A. et al. Learned sensing: jointly optimized microscope hardware for accurate image classification. *Biomed. Opt. Express* **10**, 6351–6369 (2019).
77. Horstmeyer, R., Chen, R. Y., Kappes, B. & Judkewitz, B. Convolutional neural networks that teach microscopes how to image. Preprint at https://arxiv.org/abs/1709.07223 (2017).
78. Kellman, M., Bostan, E., Chen, M. & Waller, L. in *2019 IEEE International Conference on Computational Photography (ICCP)* 1–8 (IEEE, 2017).
79. Jiang, S., Guo, K., Liao, J. & Zheng, G. Solving Fourier ptychographic imaging problems via neural network modeling and TensorFlow. *Biomed. Opt. Express* **9**, 3306–3319 (2018).
80. Sun, M. et al. Neural network model combined with pupil recovery for Fourier ptychographic microscopy. *Opt. Express* **27**, 24161–24174 (2019).
81. Zhang, Y. et al. PgNN: Physics-guided neural network for fourier ptychographic microscopy. Preprint at https://arxiv.org/abs/1909.08869 (2019).
82. Zhang, J. et al. Forward imaging neural network with correction of positional misalignment for Fourier ptychographic microscopy. *Opt. Express* **28**, 23164–23175 (2020).
83. Baydin, A. G., Pearlmutter, B. A., Radul, A. A. & Siskind, J. M. Automatic differentiation in machine learning: a survey. *J. Mach. Learn. Res.* **18**, 5595–5637 (2017).
84. Wang, R. et al. Virtual brightfield and fluorescence staining for Fourier ptychography via unsupervised deep learning. *Opt. Lett.* **45**, 5405–5408 (2020).
85. Ou, X., Chung, J., Horstmeyer, R. & Yang, C. Aperture scanning Fourier ptychographic microscopy. *Biomed. Opt. Express* **7**, 3140–3150 (2016).
86. He, X., Jiang, Z., Kong, Y., Wang, S. & Liu, C. Fourier ptychography via wavefront modulation with a diffuser. *Opt. Commun.* **459**, 125057 (2020).
87. Choi, G.-J. et al. Dual-wavelength Fourier ptychography using a single LED. *Opt. Lett.* **43**, 3526–3529 (2018).
88. He, X., Liu, C. & Zhu, J. Single-shot aperture-scanning Fourier ptychography. *Opt. Express* **26**, 28187–28196 (2018).
89. Holloway, J. et al. Toward long-distance subdiffraction imaging using coherent camera arrays. *IEEE Trans. Comput. Imaging* **2**, 251–265 (2016).
90. Guo, K., Dong, S. & Zheng, G. Fourier ptychography for brightfield, phase, darkfield, reflective, multi-slice, and fluorescence imaging. *IEEE J. Sel. Top. Quantum Electron.* **22**, 77–88 (2015).
91. Pacheco, S., Salahieh, B., Milster, T., Rodriguez, J. J. & Liang, R. Transfer function analysis in epi-illumination

Fourier ptychography. *Opt. Lett.* **40**, 5343–5346 (2015).
92. Pacheco, S., Zheng, G. & Liang, R. Reflective Fourier ptychography. *J. Biomed. Opt.* **21**, 026010 (2016).
93. Lee, H., Chon, B. H. & Ahn, H. K. Reflective Fourier ptychographic microscopy using a parabolic mirror. *Opt. Express* **27**, 34382–34391 (2019).
94. Shen, C. et al. Computational aberration correction of VIS-NIR multispectral imaging microscopy based on Fourier ptychography. *Opt. Express* **27**, 24923–24937 (2019).
95. Wojdyla, A., Benk, M. P., Naulleau, P. P. & Goldberg, K. A. in *Image Sensing Technologies: Materials, Devices, Systems, and Applications* Vol. 106560W (International Society for Optics and Photonics, 2018).
96. Chan, A. C. et al. Parallel Fourier ptychographic microscopy for high-throughput screening with 96 cameras (96 eyes). *Sci. Rep.* **9**, 11114 (2019).
97. Konda, P. C., Taylor, J. M. & Harvey, A. R. Parallelized aperture synthesis using multi-aperture Fourier ptychographic microscopy. Preprint at https://arxiv.org/abs/1806.02317 (2018).
98. Lee, B. et al. Single-shot phase retrieval via Fourier ptychographic microscopy. *Optica* **5**, 976–983 (2018).
99. He, X., Liu, C. & Zhu, J. Single-shot Fourier ptychography based on diffractive beam splitting. *Opt. Lett.* **43**, 214–217 (2018).
100. Gustafsson, M. G. Surpassing the lateral resolution limit by a factor of two using structured illumination microscopy. *J. Microsc.* **198**, 82–87 (2000).
101. Dong, S., Nanda, P., Shiradkar, R., Guo, K. & Zheng, G. High-resolution fluorescence imaging via pattern-illuminated Fourier ptychography. *Opt. Express* **22**, 20856–20870 (2014).
102. Guo, K. et al. 13-fold resolution gain through turbid layer via translated unknown speckle illumination. *Biomed. Opt. Express* **9**, 260–275 (2018).
103. Zhang, H. et al. Near-field Fourier ptychography: super-resolution phase retrieval via speckle illumination. *Opt. Express* **27**, 7498–7512 (2019).
104. Yeh, L.-H., Chowdhury, S. & Waller, L. Computational structured illumination for high-content fluorescence and phase microscopy. *Biomed. Opt. Express* **10**, 1978–1998 (2019).
105. Dong, S., Nanda, P., Guo, K., Liao, J. & Zheng, G. Incoherent Fourier ptychographic photography using structured light. *Photonics Res.* **3**, 19–23 (2015).
106. Simons, H., Poulsen, H. F., Guigay, J. & Detlefs, C. X-ray Fourier ptychographic microscopy. Preprint at https://arxiv.org/abs/1609.07513 (2016).
107. Detlefs, C., Beltran, M. A., Guigay, J.-P. & Simons, H. Translative lens-based full-field coherent X-ray imaging. *J. Synchrotron Rad.* **27**, 119–126 (2020).
108. Pedersen, A. et al. X-ray coherent diffraction imaging with an objective lens: Towards three-dimensional mapping of thick polycrystals. *Phys. Rev. Res.* **2**, 033031 (2020).
109. Cowley, J. M. & Moodie, A. F. The scattering of electrons by atoms and crystals. I. A new theoretical approach. *Acta Crystallogr.* **10**, 609–619 (1957).
110. Godden, T., Suman, R., Humphry, M., Rodenburg, J. & Maiden, A. Ptychographic microscope for three-dimensional imaging. *Opt. Express* **22**, 12513–12523 (2014).
111. Tian, L. & Waller, L. 3D intensity and phase imaging from light field measurements in an LED array microscope. *Optica* **2**, 104–111 (2015).
112. Chowdhury, S. et al. High-resolution 3D refractive index microscopy of multiple-scattering samples from intensity images. *Optica* **6**, 1211–1219 (2019).
113. Song, P. et al. Super-resolution microscopy via ptychographic structured modulation of a diffuser. *Opt. Lett.* **44**, 3645–3648 (2019).
114. Bian, Z. et al. Ptychographic modulation engine: a low-cost DIY microscope add-on for coherent super-resolution imaging. *J. Phys. D Appl. Phys.* **53**, 014005 (2019).
115. Ou, X., Horstmeyer, R., Yang, C. & Zheng, G. Quantitative phase imaging via Fourier ptychographic microscopy. *Opt. Lett.* **38**, 4845–4848 (2013).
116. Zheng, G. Breakthroughs in photonics 2013: Fourier ptychographic imaging. *IEEE Photonics J.* **6**, 0701207 (2014).
117. Horstmeyer, R., Ou, X., Zheng, G., Willems, P. & Yang, C. Digital pathology with Fourier ptychography. *Comput. Med. Imaging Graph.* **42**, 38–43 (2015).
118. Williams, A. J. et al. Fourier ptychographic microscopy for filtration-based circulating tumor cell enumeration and analysis. *J. Biomed. Opt.* **19**, 066007 (2014).
119. Kim, J., Henley, B. M., Kim, C. H., Lester, H. A. & Yang, C. Incubator embedded cell culture imaging system (EmSight) based on Fourier ptychographic microscopy. *Biomed. Opt. Express* **7**, 3097–3110 (2016).
120. Kamal, T., Yang, L. & Lee, W. M. In situ retrieval and correction of aberrations in moldless lenses using Fourier ptychography. *Opt. Express* **26**, 2708–2719 (2018).
121. Chung, J., Martinez, G. W., Lencioni, K. C., Sadda, S. R. & Yang, C. Computational aberration compensation by coded-aperture-based correction of aberration obtained from optical Fourier coding and blur estimation. *Optica* **6**, 647–661 (2019).
122. Chung, J., Kim, J., Ou, X., Horstmeyer, R. & Yang, C. Wide field-of-view fluorescence image deconvolution with aberration-estimation from Fourier ptychography. *Biomed. Opt. Express* **7**, 352–368 (2016).
123. Candes, E. J., Strohmer, T. & Voroninski, V. Phaselift: Exact and stable signal recovery from magnitude measurements via convex programming. *Commun. Pure Appl. Math.* **66**, 1241–1274 (2013).
124. Horstmeyer, R. et al. Solving ptychography with a convex relaxation. *New J. Phys.* **17**, 053044 (2015).
125. Hesse, R., Luke, D. R. & Neumann, P. Alternating projections and Douglas-Rachford for sparse affine feasibility. *IEEE Trans. Signal Process.* **62**, 4868–4881 (2014).
126. Heuke, S. et al. Coherent anti-stokes Raman Fourier ptychography. *Opt. Express* **27**, 23497–23514 (2019).
127. Goodman, J. W. *Introduction to Fourier Optics* 4th edn (Macmillan Learning, 2017).
128. Horstmeyer, R., Ou, X., Chung, J., Zheng, G. & Yang, C. Overlapped Fourier coding for optical aberration removal. *Opt. Express* **22**, 24062–24080 (2014).
129. Zhang, M., Zhang, L., Yang, D., Liu, H. & Liang, Y. Symmetrical illumination based extending depth of field in Fourier ptychographic microscopy. *Opt. Express* **27**, 3583–3597 (2019).
130. Guo, K. et al. Microscopy illumination engineering using a low-cost liquid crystal display. *Biomed. Opt. Express* **6**, 574–579 (2015).
131. Dong, S., Bian, Z., Shiradkar, R. & Zheng, G. Sparsely sampled Fourier ptychography. *Opt. Express* **22**, 5455–5464 (2014).
132. Bian, L. et al. Motion-corrected Fourier ptychography. *Biomed. Opt. Express* **7**, 4543–4553 (2016).
133. Zhang, Y., Pan, A., Lei, M. & Yao, B. Data preprocessing methods for robust Fourier ptychographic microscopy. *Optical Eng.* **56**, 123107 (2017).
134. Pan, A., Zuo, C., Xie, Y., Lei, M. & Yao, B. Vignetting effect in Fourier ptychographic microscopy. *Opt. Lasers Eng.* **120**, 40–48 (2019).
135. Zuo, C., Sun, J. & Chen, Q. Adaptive step-size strategy for noise-robust Fourier ptychographic microscopy. *Opt. Express* **24**, 20724–20744 (2016).
136. Bian, L. et al. Fourier ptychographic reconstruction using Wirtinger flow optimization. *Opt. Express* **23**, 4856–4866 (2015).
137. Bian, L. et al. Fourier ptychographic reconstruction using Poisson maximum likelihood and truncated Wirtinger gradient. *Sci. Rep.* **6**, 27384 (2016).
138. Chen, S., Xu, T., Zhang, J., Wang, X. & Zhang, Y. Optimized denoising method for fourier ptychographic microscopy based on wirtinger flow. *IEEE Photonics J.* **11**, 1–14 (2019).
139. Bostan, E., Soltanolkotabi, M., Ren, D. & Waller, L. in *2018 25th IEEE International Conference on Image Processing (ICIP)* 3823–3827 (IEEE, 2018).
140. Liu, J., Li, Y., Wang, W., Tan, J. & Liu, C. Accelerated and high-quality Fourier ptychographic method using a double truncated Wirtinger criteria. *Opt. Express* **26**, 26556–26565 (2018).
141. Zhang, Y., Song, P., Zhang, J. & Dai, Q. Fourier ptychographic microscopy with sparse representation. *Sci. Rep.* **7**, 8664 (2017).
142. Zhang, Y., Cui, Z., Zhang, J., Song, P. & Dai, Q. Group-based sparse representation for Fourier ptychography microscopy. *Opt. Commun.* **404**, 55–61 (2017).
143. Zhang, Y., Song, P. & Dai, Q. Fourier ptychographic microscopy using a generalized Anscombe transform approximation of the mixed Poisson-Gaussian likelihood. *Opt. Express* **25**, 168–179 (2017).
144. Fan, Y., Sun, J., Chen, Q., Wang, M. & Zuo, C. Adaptive denoising method for Fourier ptychographic microscopy. *Opt. Commun.* **404**, 23–31 (2017).
145. Sun, Y. et al. in *2019 IEEE International Conference on Acoustics, Speech and Signal Processing (ICASSP 2019)* 7665–7669 (IEEE, 2019).
146. Jagatap, G., Chen, Z., Nayer, S., Hegde, C. & Vaswani, N. Sample efficient fourier ptychography for structured data. *IEEE Trans. Comput. Imaging* **6**, 344–357 (2019).
147. Ling, R., Tahir, W., Lin, H.-Y., Lee, H. & Tian, L. High-throughput intensity diffraction tomography with a computational microscope. *Biomed. Opt. Express* **9**, 2130–2141 (2018).
148. Li, J. et al. High-speed in vitro intensity diffraction tomography. *Adv. Photonics* **1**, 066004 (2019).
149. Matlock, A. & Tian, L. High-throughput, volumetric quantitative phase imaging with multiplexed intensity diffraction tomography. *Biomed. Opt. Express* **10**, 6432 (2019).
150. Pham, T.-A. et al. Versatile reconstruction framework for diffraction tomography with intensity measurements and multiple scattering. *Opt. Express* **26**, 2749–2763 (2018).

**Acknowledgements**
G.Z. acknowledges the support of NSF 1510077, NSF 2012140 and the UConn SPARK grant. P.S. acknowledges the support of the Thermo Fisher Scientific Fellowship. C.Y. acknowledges the support of the Rosen Bioengineering Center Endowment Fund (9900050).

**Author contributions**
G.Z. prepared the display items. S.J. prepared the initial draft of the Supplementary Note. All authors contributed to all aspects of manuscript preparation, revision and editing.

**Competing interests**
The authors declare no competing interests.

**Peer review information**
*Nature Reviews Physics* thanks Ashok Veeraraghavan and the other, anonymous, reviewer(s) for their contribution to the peer review of this work.

**Publisher's note**
Springer Nature remains neutral with regard to jurisdictional claims in published maps and institutional affiliations.

**Supplementary information**
Supplementary information is available for this paper at https://doi.org/10.1038/s42254-021-00280-y.